*applied sciences*

MDPI

*Article*

# Damage Evolution Mechanism of Sandstone in the Tarangole Mining Area Under Varying Freeze–Thaw Cycles and Freezing Temperatures

**Jianhua Li [1,2,3], Zhibin Li [1,2,4], Sicheng Wang [1,2,*], Yongjiang Luo [1,2,*] and Xujing Tan [1,2]**

1 State Key Laboratory of Coal Mine Disaster Dynamics and Control, Chongqing University, Chongqing 400044, China; 10039064@ceic.com (J.L.); lizhibin0304@163.com (Z.L.); 20195617@cqu.edu.cn (X.T.)
2 School of Resources and Safety Engineering, Chongqing University, Chongqing 400044, China
3 China Energy Group Hangjin Energy Company Ordos, Ordos 017400, China
4 CCTEG Xi'an Research Institute (Group) Co., Ltd., Xi'an 710077, China
* Correspondence: 202220021074t@stu.cqu.edu.cn (S.W.); luoyj16@cqu.edu.cn (Y.L.)

**Abstract**

Freeze–thaw cycles cause mechanical deterioration and instability of slope rock masses in open-pit coal mines located in the cold regions of Northwest China. In this study, the research object is fine-grained sandstone from the Yan'an Formation in the Tarangole mining area of the Ordos Basin. Here, indoor freeze–thaw cycling, uniaxial compression, and triaxial compression tests were conducted to systematically analyze the deformation behavior, strength evolution, and failure modes of the sandstone under varying numbers of freeze–thaw cycles, freezing temperatures, and confining pressures, thereby revealing its freeze–thaw damage mechanism. The results show that the number of freeze–thaw cycles is the dominant factor affecting the elastic modulus. Freezing temperatures (especially between −5 °C and −15 °C) and the number of freeze–thaw cycles (particularly the first 10 cycles) significantly reduce peak strength. In addition, confining pressure can significantly enhance the resistance to deformation (under 15 freeze–thaw cycles, the elastic modulus increases by 181.8% as confining pressure rises from 0 to 2 MPa). Within the low confining pressure range (0–1.5 MPa), peak strain decreases monotonically with increasing confining pressure and is independent of the number of freeze–thaw cycles. Finally, the increase in the number of freeze–thaw cycles and the decrease in temperature jointly promote crack development, and the failure mode shifts from pure shear to a shear-tension composite mode. The underlying cause lies in the evolution of interparticle cementation within the soil skeleton and in the associated pore–crack structure. In addition, based on fracture damage mechanics and the modified Weibull distribution, a damage evolution equation and a constitutive model for sandstone considering freeze–thaw cycles and temperature effects were established and validated. Therefore, the research findings can provide a theoretical basis for slope support, freeze–thaw disaster prevention and mitigation, and stability assessment in the Tarangole mining area and other cold regions.

**Keywords:** slope stability; rock mechanics; freeze–thaw cycles; indoor mechanical test; damage evolution mechanism; constitutive model

Check for updates

Academic Editor: Nikolaos Koukouzas

Received: 26 April 2026
Revised: 7 June 2026
Accepted: 13 June 2026
Published: 17 June 2026



## 1. Introduction

Constrained by a resource endowment featuring abundant coal, insufficient oil, and scarce natural gas, coal has long held a dominant position in China's energy mix [1].

According to the medium- and long-term goals set out in the "Energy Development Strategy Action Plan (2014–2020)", coal consumption is projected to account for approximately 60% of the total energy mix by 2030 [2]. However, most of China's coal resources are buried deep underground, and the proportion of coal mines suitable for open-pit mining is relatively low [3]. By the end of 2025, China's open-pit coal mines—which account for approximately 8% of the total number of coal mines (357)—are projected to contribute about 25% of the country's total coal output (1.18 billion tons), thereby providing a significant guarantee for national energy security and the stable supply of coal resources [4,5]. The major open-pit coal mines in China are primarily located in the high-altitude, cold, and seasonally frozen regions of Inner Mongolia, Shanxi, Xinjiang, Liaoning, and Heilongjiang (Figure 1). In the high-altitude, cold winter zone, the rock mass of the open-pit coal mine's final slope is subjected to diurnal and seasonal temperature fluctuations, as well as environmental water action. When the temperature falls below 0 °C, pore water in the rock mass freezes and expands. Under the combined effects of segregated ice formation and moisture migration, the pore structure dilates, and new fractures initiate [6–8]. After the temperature rises above 0 °C, meltwater from ice seeps into newly formed pores, softening the rock mass and creating conditions for the next freeze–thaw cycle. Repeated freezing and thawing is a key cause of the continuous deterioration of the structural integrity and mechanical properties of rock masses in cold-region slopes [9,10]. Coupled with factors such as blasting, vibration, and long-term creep, this process further increases the risk of slope instability.

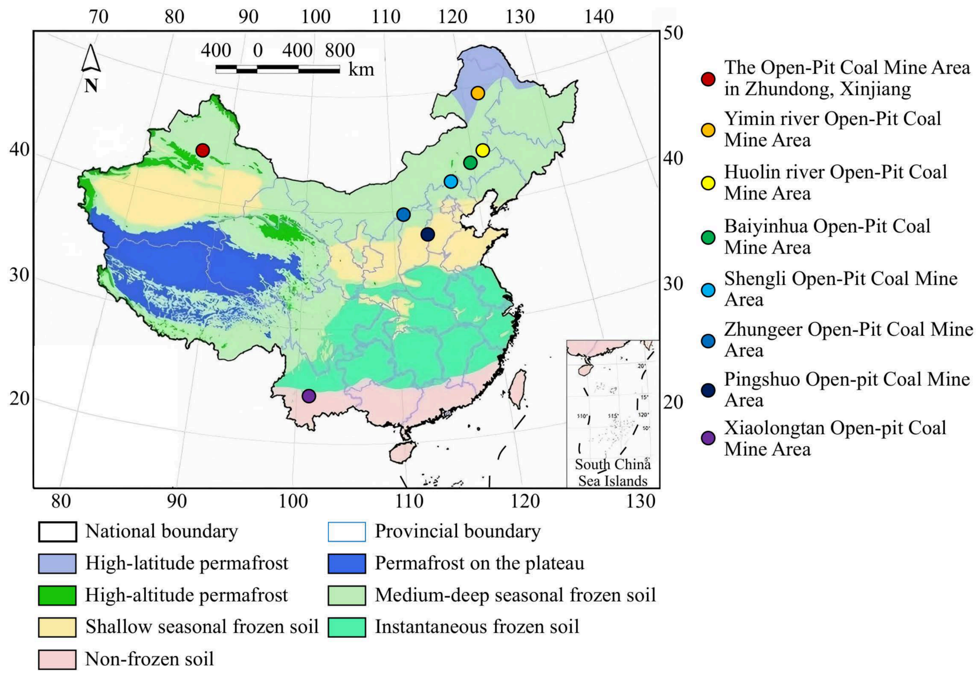


**Figure 1.** The distribution of major open-pit coal mining areas and permafrost regions in China.

The problem of slope instability in open-pit mines in China is severe. From 2011 to 2022, there were nearly 2000 slope-instability incidents in open-pit mines alone [11]. The extremely serious collapse accident at Xingjing Coal Industry in Inner Mongolia in 2023 claimed 53 lives [12]. The 2024 heap leach slope collapse at the Copler gold mine in Turkey, which killed nine people, further highlights the severity of slope instability [13]. Although the total number of mining accidents nationwide has been declining in recent years (with a year-on-year decrease of 25.6% in 2024), slope instability incidents still occur periodically, often resulting in significant casualties and economic losses [14]. The Ordos Basin is an important coal energy base in China, where weakly cemented strata of the Cretaceous and

Jurassic systems are widely distributed [15]. The Tarangole mining area is located in the northern part of the basin [16]. It experiences a long, severe winter characterized by a large diurnal temperature range and intense seasonal freeze–thaw cycles, creating typical climatic conditions conducive to freeze–thaw damage in rock masses [17]. At present, production mines such as Hongqingliang and Bojianghaizi have been established in this mining area, while mines such as Tarangole and Youfanghao are still under infrastructure construction. Meanwhile, mining scale and depth are continuously expanding [18]. Against this backdrop, the stability of slope rock masses has become an increasingly prominent area of concern due to the coupled effects of multiple factors, such as freeze–thaw cycles, blasting vibrations, and long-term creep. Additionally, engineering practices in multiple open-pit mines and transportation slopes in the northwest region have shown that such multi-factor coupling effects further intensify the progressive failure of rock mass structures [19,20]. For instance, the end-wall slope of a certain open-pit coal mine in Inner Mongolia has exhibited varying degrees of deformation, cracking, and even incipient sliding during freeze–thaw cycles [21]. Nevertheless, a systematic understanding of the damage evolution mechanism and instability criteria of typical rock masses—such as weakly cemented sandstone, mudstone, and tuff—in the cold regions of Northwest China under freeze–thaw cycles remains lacking [22]. Hence, it is urgent to conduct research on the deformation and fracture mechanisms of rock masses subjected to freeze–thaw cycles in cold regions of Northwest China, such as the Tarangole mining area.

In recent years, with the deepening implementation of China's Western Development Strategy and the Belt and Road Initiative, numerous rock–soil engineering projects in cold regions have been launched successively. Consequently, the stability of rock–soil engineering structures in cold regions has become a research hotspot in the engineering community [23]. A large number of achievements have been made in research on the damage and weakening mechanisms, failure mechanisms, and creep instability mechanisms of rock mass media under cyclic freeze–thaw conditions through physical experiments, numerical simulations, and machine learning [24]. Some scholars have investigated the peak strength of sandstones with varying initial strengths under different freeze–thaw cycles through mechanical tests and found that, as the number of freeze–thaw cycles increases, the peak strength gradually decreases and sample damage intensifies [25–32] (Figure 2a). Furthermore, the theory of segregated ice was proposed and has been gradually applied to the field of rock freeze–thaw processes, particularly in relation to frost heave in permafrost [33]. The mechanism lies in the presence of hydraulically connected unfrozen water during freezing, which drives water migration in the frozen fringe region (Figure 2b). Traditional tests have established the correlation between water moisture and freeze–thaw damage and revealed the macroscopic deterioration patterns of sandstone [34]. However, physical experiments are usually time-consuming, destructive, and incapable of capturing the microscopic mechanisms of crack initiation and propagation at the particle scale. To overcome these limitations, numerical simulations are widely used to complement experimental research. By using methods such as the finite element method (FEM) or the discrete element method (DEM), researchers can simulate both the heterogeneous internal structure of sandstone and the thermo-hydro-mechanical coupling processes occurring during freeze–thaw cycles [35–38]. These simulations enable parametric analyses that are typically difficult to perform under laboratory conditions, visualize the internal stress field, and predict crack propagation patterns under varying temperature gradients and confining pressures [39]. However, they are limited by simplified constitutive relations and the need for precise calibration of microscopic parameters, making it difficult to accurately predict the mechanical behavior of various types of sandstone.

The rise of machine learning (ML) has brought about a paradigm shift, enabling a data-driven approach to model the inherently complex, nonlinear relationships underlying the freeze–thaw deterioration process. Specifically, in contrast to laboratory tests and numerical simulation methods, ML algorithms (such as artificial neural networks (ANNs) and support vector machines (SVMs)) can automatically learn complex patterns from experimental data without requiring explicit physical equations [40,41]. These models demonstrate superior performance in predicting the macroscopic mechanical properties (e.g., compressive strength and elastic modulus) of sandstone, taking freeze–thaw cycles, porosity, and mineral composition as inputs [42]. Johnson et al. used the GloPrSM model to predict, for the first time, the quartz, feldspar, and lithic fragment contents of global river sands and found that slope, temperature, and rock type are the main controlling factors [43]. Zhou et al. accurately predicted the compressive strength of freeze–thaw rocks using a support vector regression model optimized by the chameleon swarm algorithm and found that impact pressure and characteristic impedance are the key influencing parameters [44].

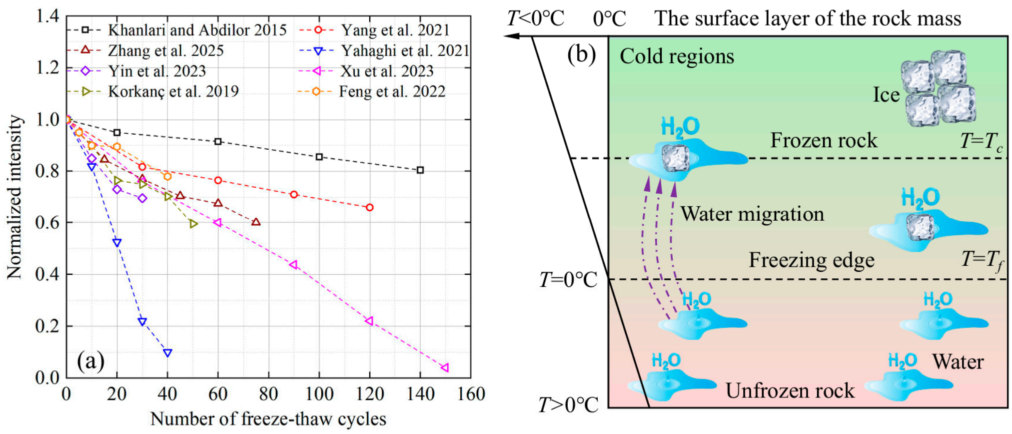


**Figure 2.** Mechanical properties of rock mass under different freeze–thaw cycles [25–32]. (**a**) Peak intensity; and (**b**) schematic diagram of water migration.

Although the aforementioned studies have conducted extensive research on mechanical testing, numerical simulation, and machine learning, they have not carried out comprehensive field investigations into the geological formations and lithological variations in the strata in the Tarangole coal mining area. Moreover, systematic studies on the damage evolution mechanism and creep behavior of the hard, thick sandstone roof in this mining area under varying freeze–thaw cycles remain lacking. This study investigates the geological structures and lithology of the strata in the Tarangole coal mining area. Additionally, mechanical property tests are conducted on roof hard thick-layer sandstone subjected to varying numbers of freeze–thaw cycles and different freezing temperatures to analyze the evolution of its strength, deformation characteristics, and macroscopic fracture morphology as functions of cycle number, freezing temperature, and confining pressure level. Finally, based on fracture damage mechanics theory and considering both the number of freeze–thaw cycles and temperature effects, a damage variable is defined, and the damage evolution equation and constitutive equation for rock subjected to freeze–thaw cycling are established. Their accuracy is then verified using experimental results. Accordingly, the research findings can not only improve the theoretical understanding of rock mass engineering stability in cold regions and enhance the prediction and early warning capabilities for slope disasters but also ensure the safe operation of major infrastructure projects.

## 2. Engineering Background

The Tarangole mining area is located in Dalad Banner, Ordos City, Inner Mongolia (Figure 3a). It has an irregular, wedge-shaped outline, extending approximately 11 km from east to west and about 9 km from north to south. The altitude within the area ranges from 1410 m to 1530 m, with a relative relief of approximately 120 m. Gullies are well developed, and the terrain is deeply incised, predominantly characterized by steep "V"-shaped valleys. The area belongs to a hilly region characterized by a mixture of soil and bedrock. The climate is dry and windy, with northwesterly winds prevailing. The maximum wind speed is 14 m/s, and the typical wind speed ranges from 2.2 m/s to 5.2 m/s [16]. As shown in Figure 3b, the freezing period in the mining area extends from November to March of the following year, with temperatures ranging from −20 °C to 0 °C and a maximum frozen soil depth of 1.71 m.

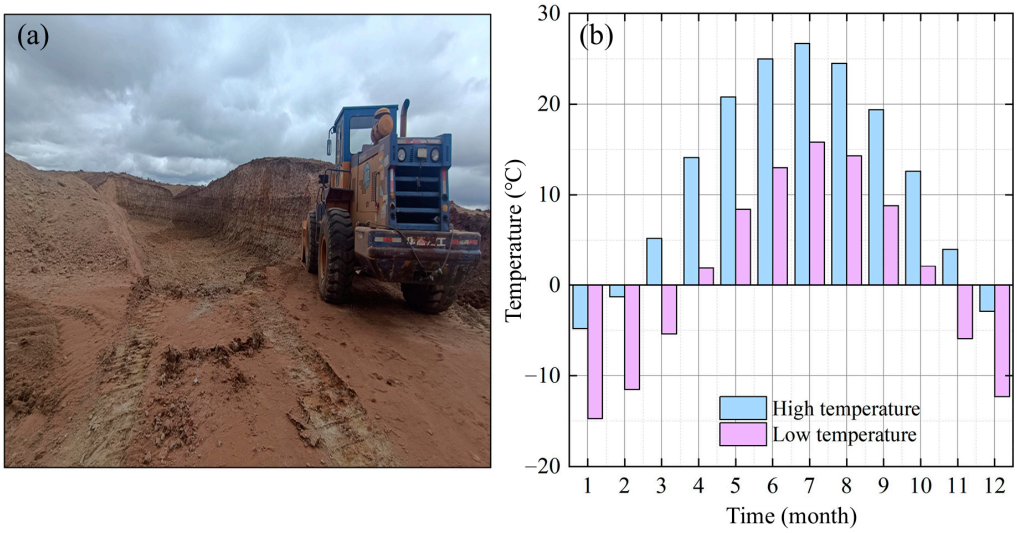


**Figure 3.** Engineering background. (**a**) Local geological map; and (**b**) the monthly average high- and low-temperature curves for the Tarangole mining area in 2024.

As demonstrated in Figure 4, the coal-bearing strata consist of mudstone, sandstones of various grain sizes, and coal seams, with sandstone accounting for approximately 80%. The Quaternary system is mainly composed of medium sandstone, fine sandstone, gravel, and clay. The ore body occurs as a tabular or lenticular body, with an attitude nearly parallel to the bedding planes; it is located 60–100 m above the contact with the underlying Ziluo Formation. Boreholes reveal three coal seams: the second coal seam, located 20–32 m below the first coal seam, has large thickness and good continuity, making it the main mineable seam; the third coal seam, located 15–21 m below the second coal seam, exhibits stable thickness and relatively good continuity, serving as the secondary mineable seam [45].

The Tarangole mining area is located at the northern edge of the Dongsheng coalfield and is characterized by a gently dipping monocline structure trending 200–250° with an inclination of 1–5°. Moreover, the dip remains relatively consistent, with only minor local undulations forming broad, gentle, wave-like folds. The area has no major faults, folds, or igneous intrusions, and its geological structure is simple. No drilling fluid leakage or structural features such as faults and folds were observed during the construction of the wellbore inspection hole.

The Tarangole coal mine is located in the northern part of the mining area, covers an area of 227.25 $m^2$, and has a designed production capacity of 10.0 Mt/a. The mining area is located on the northeastern margin of the Ordos Basin. The hydrogeological conditions are complex, and the primary direct water-bearing aquifers are the Jurassic confined aquifer and the confined aquifer within the clastic rocks of the Yan'an Formation (Figure 4). Due to numerous water inrush incidents—and even shaft flooding—during construction using the conventional method, the mine was forced to adopt the freezing method [46]. Taking the north intake and return air shafts as examples, the freezing depth of the intake air shaft is 579.60 m, and that of the return air shaft is 579.29 m. The frozen sections encompass the main water-bearing strata in the upper portions of the shafts. In addition, the mining area is located in the deep seasonal frozen soil zone of the Ordos Plateau, where large diurnal temperature variations occur in winter and spring, resulting in pronounced freeze–thaw cycles. This area was covered by continuous permafrost during the Last Glacial Maximum. Subsequently, as the climate warmed, the permafrost completely degraded, leaving behind cryogenic structures such as frost-heave wrinkles and sand wedges [47]. The research on the freeze–thaw behavior of sandstone in the region shows that when the moisture content is below 11%, frost heave is negligible. When the moisture content ranges from 12% to 16%, the frost-heave rate increases linearly and positively with moisture content and also increases with decreasing dry density and decreasing cold-end temperature [48]. At the same time, the burnt rock formed by spontaneous combustion of coal seams is prone to inducing slope instability under the influence of freeze–thaw cycles and surface water infiltration. Thus, the mining area must address two aspects simultaneously: first, accurately determining the mechanical parameters of frozen soil during artificial ground freezing construction; and second, mitigating the degradation caused by seasonal freeze–thaw cycles on the mechanical properties of rock and soil in surface engineering projects—such as slope stability.

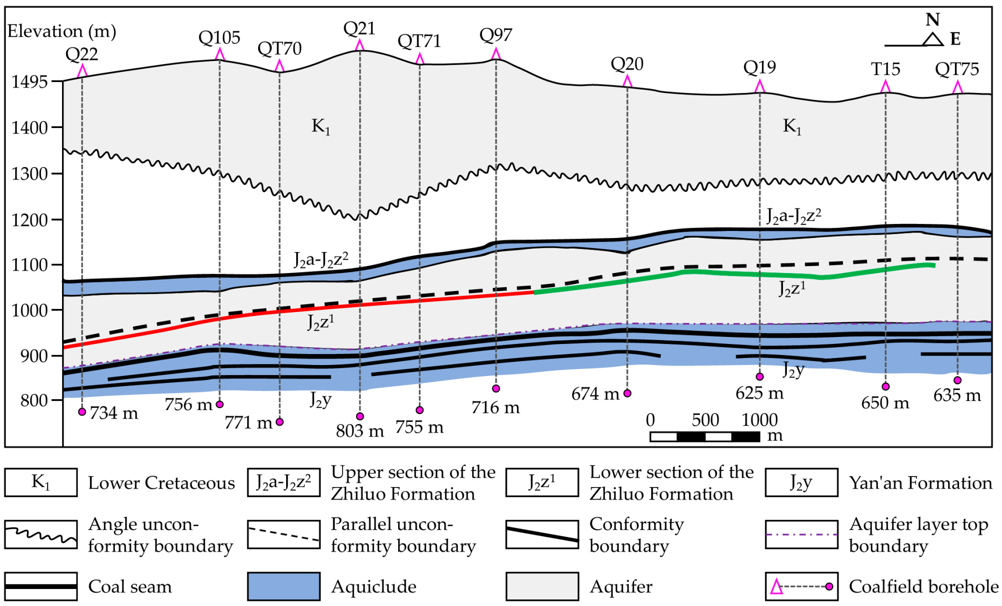


**Figure 4.** Hydrogeological profile of the Tarangole area.

## 3. Methods

In previous studies, the strength of fine sandstone in the Yan'an Formation of the Tarangole coal mining area was found to be higher than that of the Ziluo Formation. Additionally, the strength of fine sandstone was greater than that of coarse sandstone [16]. Accordingly, this research focuses on analyzing the influence of freeze–thaw cycles and freeze–thaw temperatures on the mechanical properties of fine-grained sandstone from the Yan'an Formation under uniaxial and triaxial compression testing.

### 3.1. Freeze–Thaw Cyclic Test

The freeze–thaw cyclic test on standard fine sandstone samples (50 mm × 100 mm) from the Yan'an Formation was conducted using an automatic low-temperature freezing–thawing testing system. This system allows arbitrary customization of the freeze–thaw cycle parameters, including the temperature range, number of cycles, cooling and heating rates, and duration of temperature maintenance. Here, it enables fully automatic, batch-wise control of the freeze–thaw process. The freeze–thaw cycle test is conducted as follows:

(1) The temperature range for the freeze–thaw cycle test of the sample is set to −5 °C to −20 °C; the heating and cooling rates, the dwell time at each freezing temperature (−5 °C, −10 °C, −15 °C, and −20 °C), the melting temperature (20 °C), and the number of freeze–thaw cycles (N = 5, 10, 15, or 20) are also specified. The temperature range setting refers to the actual seasonal freeze–thaw temperatures in the Tarangole mining area.
(2) The saturated rock samples in the environmental chamber of the freeze–thaw system are placed according to the specified temperature range requirements for freeze–thaw cycling, and the freeze–thaw program is initiated until the required number of cycles is completed.
(3) The rock samples that have completed the required freeze–thaw cycles should be removed from the environmental chamber of the freeze–thaw system and stored for the next test.

### 3.2. Uniaxial and Triaxial Loading Test

As depicted in Figure 5, this experiment employed the MTS815 electro-hydraulic servo rock testing system to conduct uniaxial compression tests on sandstone samples, aiming to investigate how their strength and deformation behavior evolve with the number of freeze–thaw cycles and the freezing temperature. This testing machine is mainly composed of key systems, including the program control system, the loading system, and the measurement system. Its maximum axial loading capacity is 1700 kN, and it achieves high precision in test force measurement (±0.5%), displacement measurement (±0.5%), and deformation measurement (±0.5%). Furthermore, the sampling time interval is 0.1 s. Additionally, the testing machine supports force- and displacement-controlled loading, meeting the requirement for uniform-speed loading. Specifically, circumferential strain is monitored using the American-made Epsilon 3354 extensometer (Epsilon Technology Corp., Jackson, WY, USA), which has an accuracy of ±0.0001 mm, an operating temperature range of −40 °C to 100 °C, and a sampling frequency of 10 Hz [49]. In addition, triaxial compression tests were conducted on sandstone samples after freeze–thaw cycling using the MTS815 electro-hydraulic servo rock testing system (Figure 5). Specifically, the maximum confining pressure is 45 MPa, and the data acquisition frequency is 5 kHz.

### 3.3. Test Scheme

In this study, the MTS815 electro-hydraulic servo rock testing system was used to investigate the deformation and fracture behavior of fine sandstone samples from the Yan'an Formation in the Tarangole coal mining area under varying confining pressures, freeze–thaw cycles, and freezing temperatures. Based on the historical average temperature variations in the study area, this experiment established four freeze–thaw cycle conditions for sandstone: 5, 10, 15, and 20 cycles. Four preset freezing temperatures were applied: −5 °C, −10 °C, −15 °C, and −20 °C. Furthermore, a room temperature of 20 °C served as the control condition. Uniaxial compression tests were performed on samples under each combination of freezing temperature ($T$) and freeze–thaw cycle number ($N$). A total of 20 test groups were designed, with each group replicated twice, requiring 40 samples in total.

**Figure 5.** The MTS815 electro-hydraulic servo rock testing system.

On the other hand, to investigate the influence of confining pressure on the mechanical properties and fracture behavior of sandstone under different freeze–thaw cycles, the freezing temperature was fixed at −5 °C in this test (our previous research identified this temperature as optimal for on-site construction [16]), and confining pressures were set to 1.0 MPa, 1.5 MPa, and 2.0 MPa [50]. Triaxial compression tests were conducted under 5, 10, 15, and 20 freeze–thaw cycles, respectively. A total of 16 test groups were established, with each group replicated three times, requiring 48 samples in total. It should be noted that, to ensure the accuracy of the test data, after each group of tests, the dataset exhibiting the greatest dispersion in the results is excluded, and the remaining two datasets are used as the final results for analysis. The specific experimental protocol is shown in Table 1.

**Table 1.** Test scheme.

| Freeze–Thaw Cycles ($N$) | Freezing Temperature ($T$) (°C) | Confining Pressure ($\sigma_3$) (MPa) |
|---|---|---|
| 5 | 20, −5, −10, −15, −20 | 0 |
| 10 | 20, −5, −10, −15, −20 | 0 |
| 15 | 20, −5, −10, −15, −20 | 0 |
| 20 | 20, −5, −10, −15, −20 | 0 |
| 5 | −5 | 1.0, 1.5, 2.0 |
| 10 | −5 | 1.0, 1.5, 2.0 |
| 15 | −5 | 1.0, 1.5, 2.0 |
| 20 | −5 | 1.0, 1.5, 2.0 |

## 4. Results

### *4.1. Deformation and Strength of Sandstone Under Freeze–Thaw Cycles and Temperatures*

#### 4.1.1. Characteristics of the Stress–Strain Curve

Figure 6 presents the stress–strain curves of fine-grained sandstone samples from the Yan'an Formation in the Tarangole coal mining area under different freeze–thaw cycles and freezing temperatures. Representative stress–strain curves selected from these are shown in Figure 7. Figures 6 and 7 show that, firstly, when the number of freeze–thaw cycles is 5 and 10, the stress–strain curves at each freezing temperature all exhibit four stages: compaction, approximately linear elasticity, nonlinear crack propagation, and post-peak softening. After the peak stress, there is an instantaneous drop, indicating typical brittle failure—characteristic of Type A behavior. Furthermore, when the number of freeze–thaw cycles is 10 or 20, the curve shape at each temperature remains identical to that observed under fewer cycles; nevertheless, post-peak fluctuations diminish, indicating ductile failure behavior—characteristic of Type B curves. Finally, when the freezing temperature is −5 °C or −10 °C, the stress–strain curve characteristics of the sandstone samples are essentially similar to those of Type A curves. Nevertheless, when the freezing temperature is −15 °C or −20 °C, the overall stress–strain curve characteristics are essentially similar to those of Type B curves.

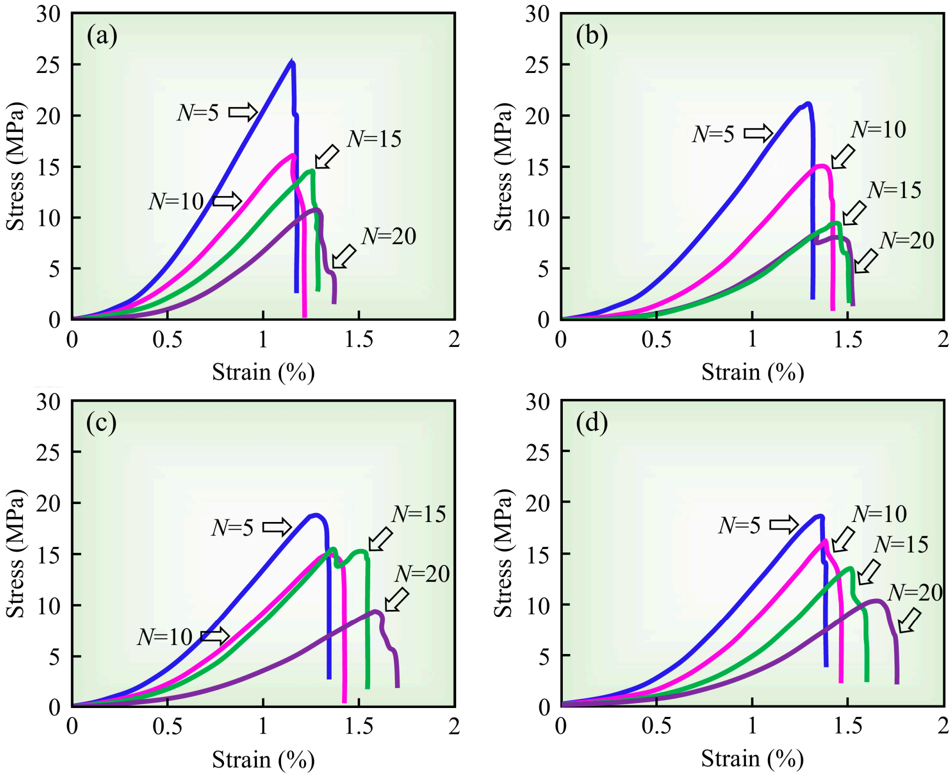


**Figure 6.** Stress–strain curves of sandstone samples under different *N* and *T*. (**a**) *T* = −5 °C; (**b**) *T* = −10 °C; (**c**) *T* = −15 °C; and (**d**) *T* = −20 °C.

The characteristics of the four stages of the typical stress–strain curve in Figure 7 are summarized as follows:

(1) Compaction stage 1: In this stage, the primary cracks and pores in the fine-grained sandstone samples gradually close. Therefore, the influence of the number of freeze–thaw cycles and the freezing temperature is reflected in the differing proportions observed during the full-loading stage.

(2) Near-linear elastic stage 2: During this stage, the internal cracks in the fine-grained sandstone samples exhibit stable propagation, and few new cracks form.

(3) Nonlinear crack propagation stage 3: In this stage, rapid and unstable propagation of internal cracks in the sandstone is observed. Here, the emergence of numerous new cracks leads to intensified overall deformation of the sample. Nevertheless, because no dominant crack channel has yet formed to penetrate the sample, it maintains its structural integrity and exhibits a dynamic equilibrium state.

(4) Post-peak stage 4: In type A curves, cracks propagate and penetrate rapidly, causing the stress to drop instantaneously; in type B curves, frost heave inhibits crack propagation, resulting in gradual crack penetration and fluctuating, gradually decreasing stress.

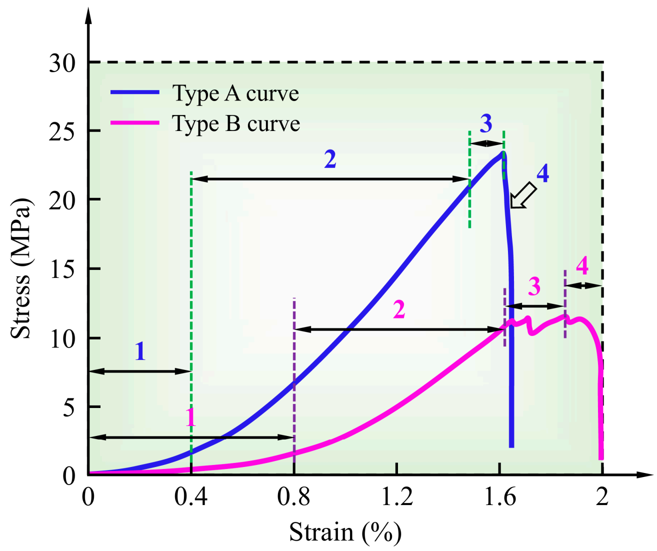


**Figure 7.** Typical stress–strain curve.

4.1.2. Elastic Modulus

Based on the characteristics of the stress–strain curve, this research adopts the secant modulus measured at 40% to 60% of the peak stress as the elastic modulus. Figure 8 shows the elastic modulus ($E$) of sandstone samples subjected to different freeze–thaw cycles and freezing temperatures, with the average elastic modulus of 2.096 GPa measured at room temperature (20 °C) serving as the control value. When the number of freeze–thaw cycles is fixed, the elastic modulus decreases exponentially as the freezing temperature decreases, and the rate of decrease gradually slows down, exhibiting a distinct interval effect (Figure 8a). Taking $N = 10$ as an example, the initial modulus at 20 °C is 2.096 GPa. It drops to 1.802 GPa at $T = -5$ °C (a decrease of 14.03%); further decreases to 1.601 GPa at $T = -10$ °C (a decrease of 11.15% relative to −5 °C); drops to 1.551 GPa at $T = -15$ °C (a decrease of only 3.12% relative to −10 °C); and decreases to 1.439 GPa at $T = -20$ °C (a decrease of 7.22% relative to −15 °C). It can be seen that the elastic modulus decline slows down in the low-temperature range (below −10 °C).

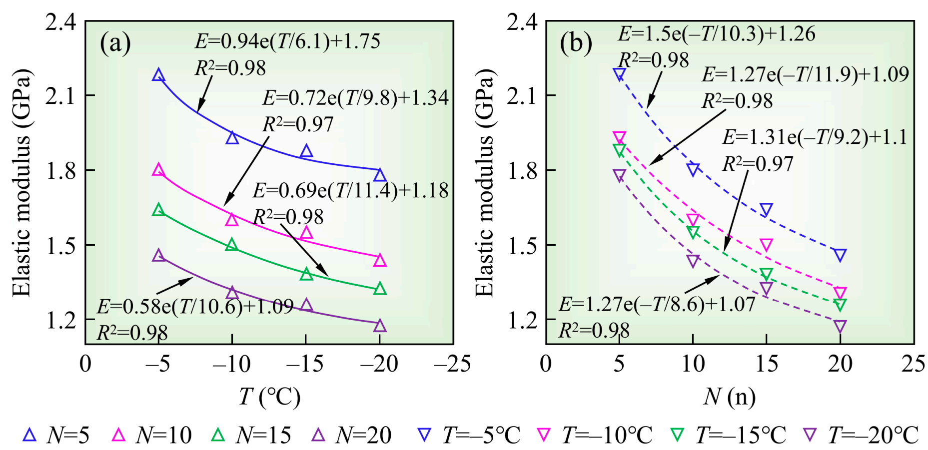


**Figure 8.** The variation characteristics of the elastic modulus ($E$) of sandstone samples with respect to the number of $T$ and $N$. (**a**) The curve of $E$ versus $T$; and (**b**) the curve of $E$ versus $N$.

On the other hand, when the freezing temperature is fixed, the elastic modulus decreases significantly with increasing number of freeze–thaw cycles (Figure 8b). Taking $T = -15$ °C as an example, when $N = 5$, the value drops to 1.878 GPa (a decrease of 10.40% from the initial value); when $N = 10$, it drops to 1.551 GPa (a decrease of 17.41% from the

$N$ = 5 value); when $N$ = 15, it drops to 1.381 GPa (a decrease of 10.96% from the $N$ = 10 value); when $N$ = 20, it drops to 1.258 GPa (a decrease of 8.91% from the $N$ = 15 value). For every increase of five cycles, the average reduction is approximately 12%, and this pattern remains largely consistent across different freezing temperatures. Therefore, the number of freeze–thaw cycles has a more pronounced weakening effect on the elastic modulus of fine sandstone than freezing temperature does, and it is the dominant factor affecting the rock's anti-deformation capacity.

#### 4.1.3. Peak Strength

Figure 9 demonstrates the relationship between the mean peak strength ($\sigma_c$) of fine sandstone samples from the Yan'an Formation in the Tarangole coal mining area and both the number of freeze–thaw cycles and the freezing temperature. Under ambient temperature (20 °C), the average peak strength of the sandstone samples is 28.67 MPa. Rock strength standards are primarily determined through laboratory testing of mechanical parameters, mainly obtained from uniaxial and triaxial compression tests. These mainly include elastic modulus, peak strain, compressive strength, cohesion, and internal friction angle. Furthermore, strength parameters under freeze–thaw conditions were obtained through freeze–thaw cycles, confining pressure tests, and post-freeze–thaw mechanical testing.

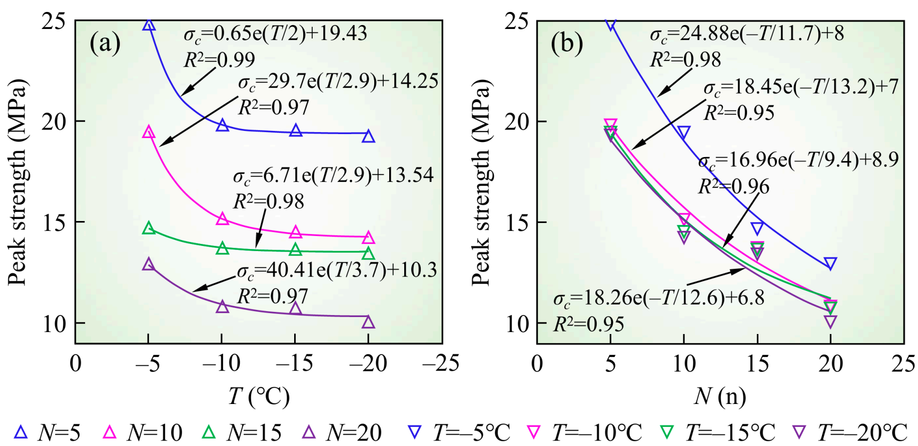


**Figure 9.** The variation characteristics of the peak strength ($\sigma_c$) of sandstone samples with respect to the number of $T$ and $N$. (**a**) The curve of σc versus $T$; and (**b**) the curve of $\sigma_c$ versus $N$.

As shown in Figure 9a, regardless of the number of freeze–thaw cycles, the peak strength decreases sharply at first and then gradually declines as the freezing temperature drops. Taking the freeze–thaw cycle number $N$ = 10 as an example, when the freezing temperature decreases from 20 °C to −5 °C, the peak strength drops to 24.86 MPa (a reduction of 13.3%); when it decreases to −10 °C, the peak strength decreases to 19.48 MPa (a reduction of 21.64%); as it decreases to −15 °C, the peak strength decreases to 14.73 MPa (a reduction of 24.38%); and when it decreases to −20 °C, the peak strength decreases to 12.96 MPa (a reduction of 12%). In general, the impact of freezing temperatures shows a distinct interval effect: it is significant in the range of −5 °C to −15 °C but weakens in the range of −15 °C to −20 °C. This rule is broadly consistent with the influence of freezing temperature on elastic modulus; nevertheless, peak strength is more sensitive to freezing temperature.

Figure 9b shows that the peak strength decreases rapidly with increasing number of freeze–thaw cycles. Taking $T$ = −15 °C as an example: after 5 and 10 cycles, the peak strength drops to 24.85 MPa (a decrease of 13.3%) and 19.85 MPa (a decrease of 20.1%), respectively; thereafter, the rate of decrease slows markedly, while after 15 and 20 cycles, it further declines to 19.57 MPa (a decrease of 1.4% relative to the value after 10 cycles) and

19.31 MPa (a decrease of 1.3% relative to the value after 15 cycles), respectively. It can be seen that the number of freeze–thaw cycles has a significant overall effect on peak strength, with the most pronounced decline occurring in the first 10 cycles. Subsequently, the decline tends to level off. This characteristic is consistent with the trend in elastic modulus, but peak strength is more sensitive to the number of cycles—similar to how freezing temperature influences the behavior.

Overall, both freezing temperature and the number of freeze–thaw cycles significantly reduce the peak strength of sandstone, and the peak strength is more sensitive to these two factors than the elastic modulus is. Within the temperature range of −5 °C to −15 °C, freezing exerts the greatest influence, and the effect of freeze–thaw cycles is predominantly observed within the first 10 cycles.

#### 4.1.4. Peak Strain

In this research, curves were plotted showing how the average peak strain ($\varepsilon_c$) of fine sandstone samples from the Tarangole area varies with the number of freeze–thaw cycles and the freezing temperature (see Figure 10). Mechanical experimental data show that the maximum absolute error and standard deviation are only 0.196% and 0.135%, respectively, confirming the homogeneity of the sandstone samples.

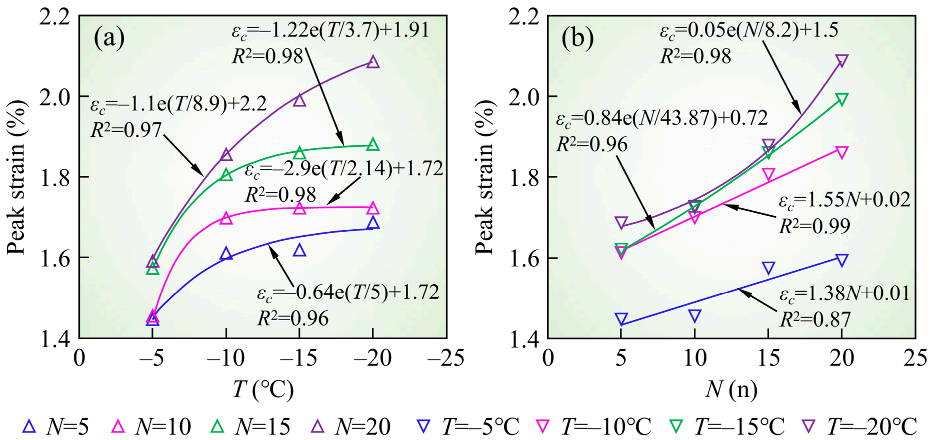


**Figure 10.** The variation characteristics of the peak strain ($\varepsilon_c$) of sandstone samples with respect to the number of $T$ and $N$. (**a**) The curve of $\varepsilon_c$ versus $T$; and (**b**) the curve of $\varepsilon_c$ versus $N$.

Regardless of the number of freeze–thaw cycles, the peak strain increases in a quasi-exponential manner as the freezing temperature decreases; nevertheless, the growth rate gradually slows down (Figure 10a). Taking $N$ = 10 as an example, when the temperature decreases from −5 °C to −10 °C, the peak strain increases from 1.46% to 1.67% (+14.4%); when it decreases to −15 °C, the peak strain increases to 1.72% (+3.0%); and when it decreases to −20 °C, it increases to 1.73% (+0.6%). In addition, the influence of freezing temperature is positively correlated with the number of freeze–thaw cycles: strain change is relatively small at low cycle numbers ($N$ = 5, 10) but becomes more pronounced at high cycle numbers ($N$ = 15, 20), indicating that under repeated freeze–thaw loading at low temperatures, sandstone is more likely to transition from brittle to ductile behavior.

On the other hand, regardless of the freezing temperature, the peak strain gradually increases with the number of freeze–thaw cycles (Figure 10b). Taking $T$ = −15 °C as an example, when the number of cycles increases from 5 to 10, the strain increases from 1.62% to 1.72% (+6.2%). Furthermore, from 10 to 15, it increases to 1.86% (+8.1%), and from 15 to 20, it increases to 1.99% (+7.0%). Meanwhile, the influence of freeze–thaw cycles on sandstone is governed by the freezing temperature, indicating that lower temperatures tend to intensify the brittle-to-ductile transition in sandstone. Therefore, this is consistent with the post-peak fluctuation characteristics observed in the stress–strain curve.

### *4.2. Deformation and Strength of Sandstone Under Confining Pressure*

To investigate the influence of confining pressure levels on the deformation behavior and strength of fine-grained sandstone samples from the Yan'an Formation in the Tarangole coal mining area under freeze–thaw conditions, the freezing temperature was fixed at −5 °C. Stress–strain curves, peak strength, elastic modulus, and peak strain of the rock samples were analyzed as functions of the number of freeze–thaw cycles and the confining pressure level.

#### 4.2.1. Characteristics of the Stress–Strain Curve

Figure 11 demonstrates the stress–strain curves of sandstone samples subjected to different numbers of freeze–thaw cycles and varying confining pressures. Figure 11 depicts that, except under uniaxial loading, the stress–strain curves of sandstone under different confining pressures—both before and after freeze–thaw cycling—exhibit five distinct stages: compaction, linear elasticity, pre-peak yielding, post-peak softening, and residual strength. This indicates that the overall morphology of the curves is largely independent of the confining pressure level. Nevertheless, regardless of the number of freeze–thaw cycles, the peak strength, elastic modulus, and peak strain all increase significantly with increasing confining pressure. In addition, as the confining pressure decreases, the compaction stage becomes more pronounced, whereas the linear elastic stage becomes shorter and less steep. Furthermore, the pre-peak yield point disappears, the post-peak stress drops sharply, and brittleness increases.

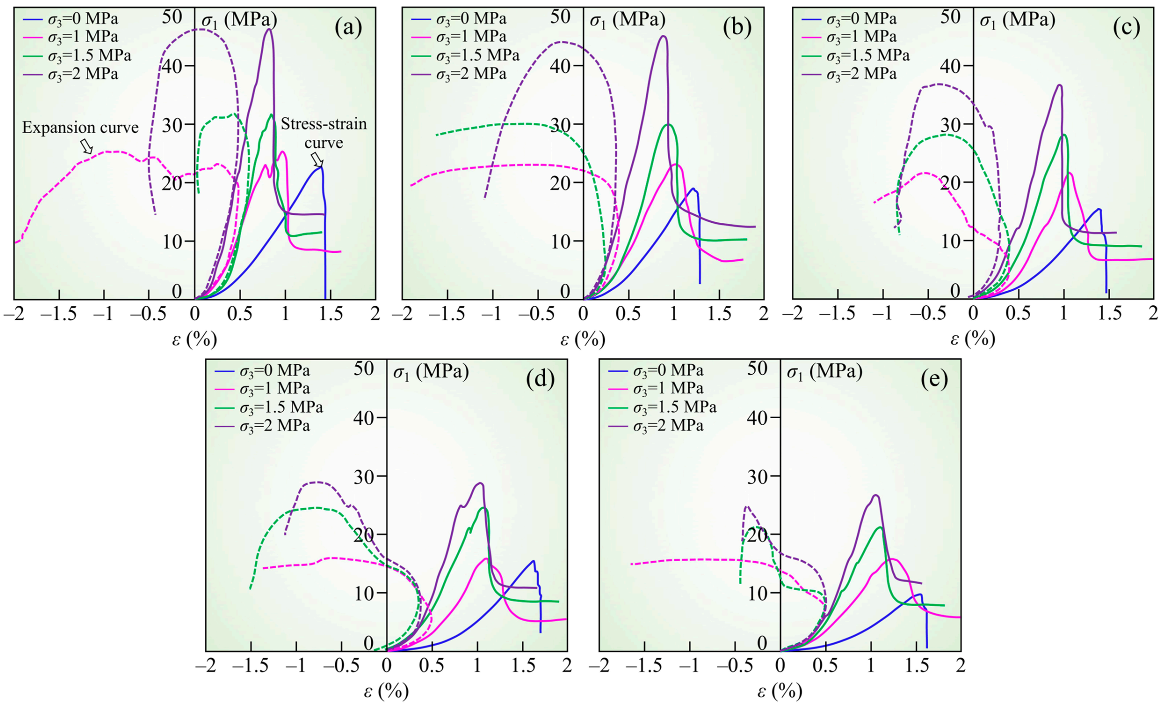


**Figure 11.** Stress–strain curves of sandstone samples under different $\sigma_3$ and $N$ (Note: the dashed line represents the expansion curve, and the solid line represents the stress–strain curve). (**a**) $N = 0$; (**b**) $N = 5$; (**c**) $N = 10$; (**d**) $N = 15$; and (**e**) $N = 20$.

#### 4.2.2. Elastic Modulus

Figure 12a shows the variation curves of the mean elastic modulus of fine sandstone samples from the Yan'an Formation in the mining area under different freeze–thaw cycles and confining pressure levels. The relationship between the fitting slope ($k$) of this curve and the number of freeze–thaw cycles is shown in Figure 12b. Under different freeze–thaw cycles, the elastic modulus of fine-grained sandstone increases approximately linearly with increasing confining pressure (Figure 12a). In this study, taking $N$ = 15 as an example, when the confining pressure increases from 0 MPa to 2 MPa, the mean elastic modulus rises from 1.48 GPa to 4.17 GPa (an 181.8% increase). This fully demonstrates that confining pressure significantly enhances the resistance to deformation. At the same time, the degree of influence of confining pressure is closely related to the number of freeze–thaw cycles. When the number of freeze–thaw cycles was 0, 5, or 10, the fitted slope of the elastic modulus versus confining pressure was relatively large; whereas when the number of freeze–thaw cycles was 15 or 20, the slope decreased significantly (the latter being approximately 60% of the former) (Figure 12b). This is because multiple freeze–thaw cycles intensify internal structural damage to the sample, weaken the load-bearing capacity of the skeletal particles, and reduce the sensitivity of the anti-deformation capability to confining pressure, thereby slowing its growth.

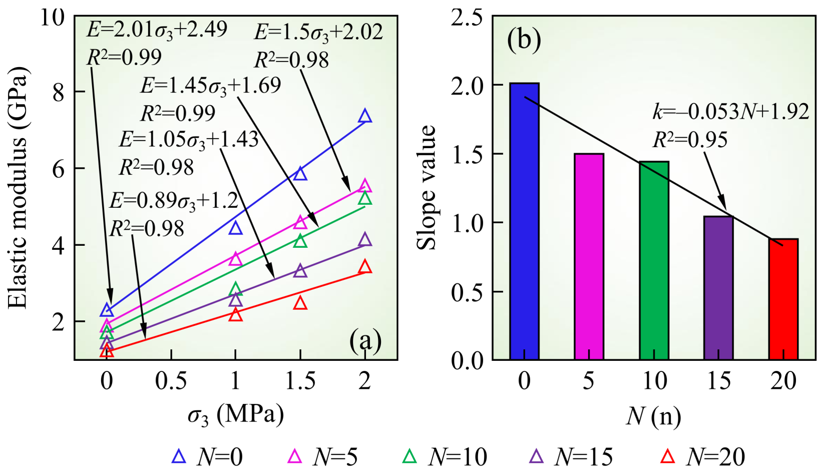


**Figure 12.** The variation characteristics of the elastic modulus of sandstone samples with respect to $N$ and $\sigma_3$. (**a**) The variation in $E$ with respect to $N$ and $\sigma_3$; and (**b**) the variation in the $k$ of the fitting curve with respect to $N$.

#### 4.2.3. Peak Strength

Under each freeze–thaw cycle, the peak strength of the fine-grained sandstone from the Yan'an Formation in the Tarangole coal mining area increases approximately linearly with increasing confining pressure (Figure 13a). Furthermore, this growth trend is independent of the number of freeze–thaw cycles; however, the strengthening effect of confining pressure is overall significant. Nevertheless, as the number of freeze–thaw cycles increases, the slope of the peak strength versus confining pressure curve gradually decreases (Figure 13b). For instance, when the number of freeze–thaw cycles was 0 and 5, the slope was approximately 9.6–10.3; it dropped to 7.9 at 10 cycles and further decreased to 6.5–6.3 at 15 and 20 cycles. Thus, this indicates that, under a low number of freeze–thaw cycles, the confining pressure reinforcement effect is more pronounced. However, when the number of freeze–thaw cycles is high, internal damage to the samples becomes severe, and the sensitivity of the confining pressure enhancement decreases significantly.

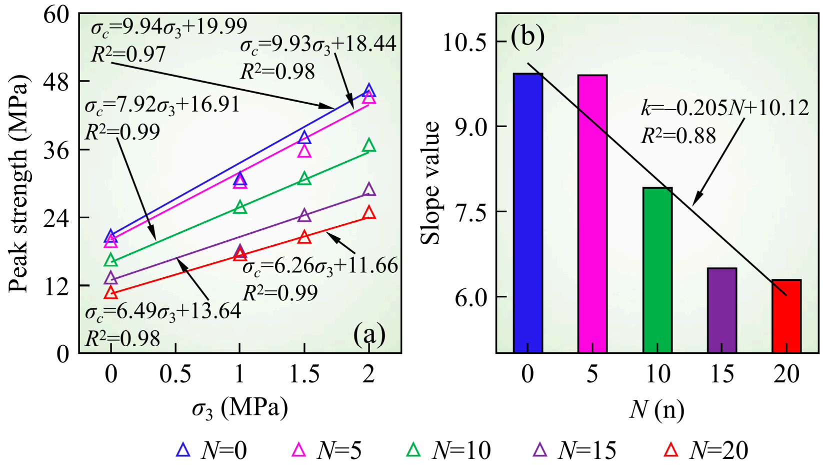


**Figure 13.** The variation characteristics of the peak strength of sandstone samples with respect to $N$ and $\sigma_3$. (**a**) The variation in $\sigma_c$ with respect to $N$ and $\sigma_3$; and (**b**) the variation in the $k$ of the fitting curve with respect to $N$.

#### 4.2.4. Peak Strain

As demonstrated in Figure 14, the variation in the average peak strain of fine-grained sandstone from the Yan'an Formation in the Tarangole coal mining area under different freeze–thaw cycles and varying confining pressure levels is presented. For each freeze–thaw cycle, the average peak strain of fine-grained sandstone decreases with increasing confining pressure, and the magnitude of this decrease gradually diminishes. For instance, when the number of freeze–thaw cycles is 5: as the confining pressure increases from 0 to 1 MPa, the peak strain decreases from 1.71% to 1.26%, representing a reduction of 26.32%; as it further increases to 1.5 MPa, the peak strain drops to 1.15%, representing an additional reduction of 8.73%; and finally, as it increases to 2 MPa, the peak strain decreases to 1.12%, representing a further reduction of only 2.61%. A similar variation pattern is observed when the number of freeze–thaw cycles is 15.

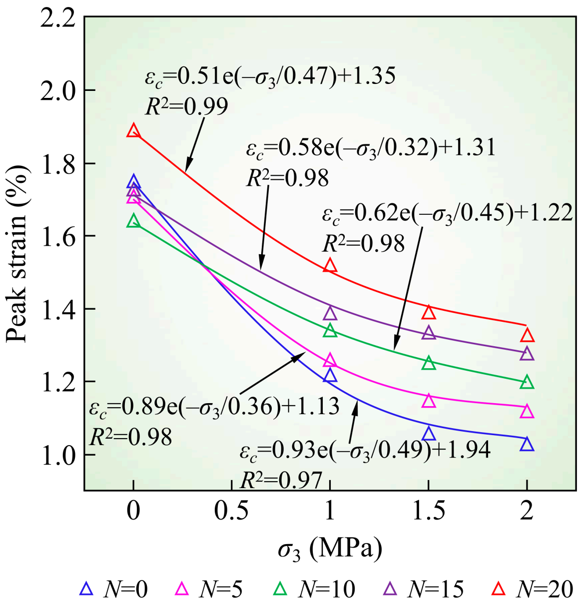


**Figure 14.** The variation rule of the $\varepsilon_c$ of sandstone samples with respect to $\sigma_3$ under different $N$.

The above analysis indicates that the peak strain of the fine-grained sandstone sample varies with confining pressure, and this trend is largely independent of the number of freeze–thaw cycles. Nevertheless, the peak strain value is highly sensitive to confining pressure. Within the low confining pressure range of 0–1.5 MPa, the peak strain of the samples decreases markedly with increasing confining pressure. However, within the relatively high confining pressure range of 1.5–2.0 MPa, this trend tends to flatten, and the influence weakens.

### *4.3. Macroscopic Failure Characteristics of Sandstone Under Freeze–Thaw Cycles*

#### 4.3.1. Macroscopic Failure Characteristics

The deformation and fracture characteristics of sandstones can reveal the mechanisms of micro-fracture initiation, propagation, and coalescence within the rock mass—information critical for understanding local instability near the unloading-relaxation zone and along structural planes in rock slopes [51,52]. In this subsection, the typical macroscopic fracture morphologies of fine-grained sandstone subjected to different freeze–thaw cycles and freezing temperatures are presented in Figure 15.

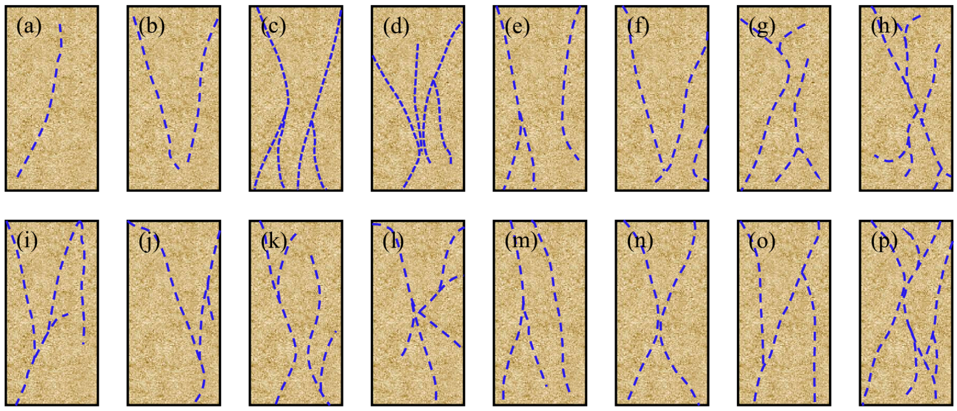


**Figure 15.** The typical macroscopic failure characteristics of fine-grained sandstone samples from the study area. (**a**) $T = -5$ °C, $N = 5$; (**b**) $T = -5$ °C, $N = 10$; (**c**) $T = -5$ °C, $N = 15$; (**d**) $T = -5$ °C, $N = 20$; (**e**) $T = -10$ °C, $N = 5$; (**f**) $T = -10$ °C, $N = 10$; (**g**) $T = -10$ °C, $N = 15$; (**h**) $T = -10$ °C, $N = 20$; (**i**) $T = -15$ °C, $N = 5$; (**j**) $T = -15$ °C, $N = 10$; (**k**) $T = -15$ °C, $N = 15$; (**l**) $T = -15$ °C, $N = 20$; (**m**) $T = -20$ °C, $N = 5$; (**n**) $T = -20$ °C, $N = 10$; (**o**) $T = -20$ °C, $N = 15$; and (**p**) $T = -20$ °C, $N = 20$.

As depicted in Figure 15, under uniaxial compression, the failure mode of fine-grained sandstone is predominantly shear failure. With an increasing number of freeze–thaw cycles and decreasing freezing temperatures, tensile cracks gradually increase, and the failure mode evolves into a shear-tensile composite failure. Under different freeze–thaw cycle temperature conditions, as the number of freeze–thaw cycles increases, the degree of damage to fine-grained sandstone gradually intensifies, and the failure mode evolves from pure shear failure to a shear-tensile composite failure. Concurrently, the angle between the main crack on the sample surface and the loading axis progressively increases. In detail, when the number of freeze–thaw cycles is 5 or 10, the degree of damage is relatively small, primarily manifesting as either single inclined-plane shear failure or "X"-shaped conjugate inclined-plane shear failure. Here, the angle between the failure surface and the loading axis ranges from 5° to 20°, and only a few localized splitting cracks are observed (Figure 15a,b). Furthermore, when the number of cycles increases to 15 and 20, the degree of damage significantly increases. The damage pattern remains predominantly single inclined-plane shearing or conjugate inclined-plane shearing in an "X" shape (Figure 15c,d). Accordingly, it can be found that the number of freeze–thaw cycles significantly affects the macroscopic fracture characteristics of fine-grained sandstone. An increase in the number of loading cycles intensifies damage to the rock sample, causing the failure mode to shift from pure shear to a combined tensile-shear mode, and the angle between the fracture surface and the loading axis to increase slightly. The mechanism lies in the fact that the frost-heaving effect enlarges the pores of the sandstone matrix [53]. After multiple freeze–thaw cycles, the matrix itself undergoes deformation and displacement, leading to progressive damage and deterioration of its mechanical properties. Macroscopically, this manifests as a change in the failure mode.

Under any number of freeze–thaw cycles, as the freezing temperature decreases, the number of surface cracks in the rock samples increases, and the extent of damage gradually intensifies. When the freezing temperature is −5 °C, the degree of damage is relatively small, with mostly single or multiple independent cracks developing on the surface. Moreover, the mechanical properties remain relatively good, and the internal structure exhibits little change (Figure 15a–d). As the freezing temperature drops to −10 °C or lower, cracks increase significantly, merge, and intersect to form conical fractures, greatly reducing the sample's structural integrity (Figure 15e–h). The main reason for this is that the decrease in freezing temperature weakens the cementation between the matrix particles, leading to a reduction in strength [54]. Therefore, overall, both the number of freeze–thaw cycles and the freezing temperature significantly influence the macroscopic failure mode of the samples.

#### 4.3.2. Internal Failure Mechanism

The influence of freeze–thaw cycles and freezing temperature on the strength variation and macroscopic failure behavior of fine-grained sandstone from the Yan'an Formation in the Tarangole coal mining area is primarily reflected in the evolution of the cementation state between framework particles and the pore–crack structure (Figure 16). In this research, the evolutionary process is divided into six stages: the natural state, the saturated state, the first freeze stage, the first thaw stage, repeated freezing, and multiple freeze–thaw cycles. The intrinsic mechanisms responsible for the differences in strength and failure characteristics during gradual changes at each stage are as follows.

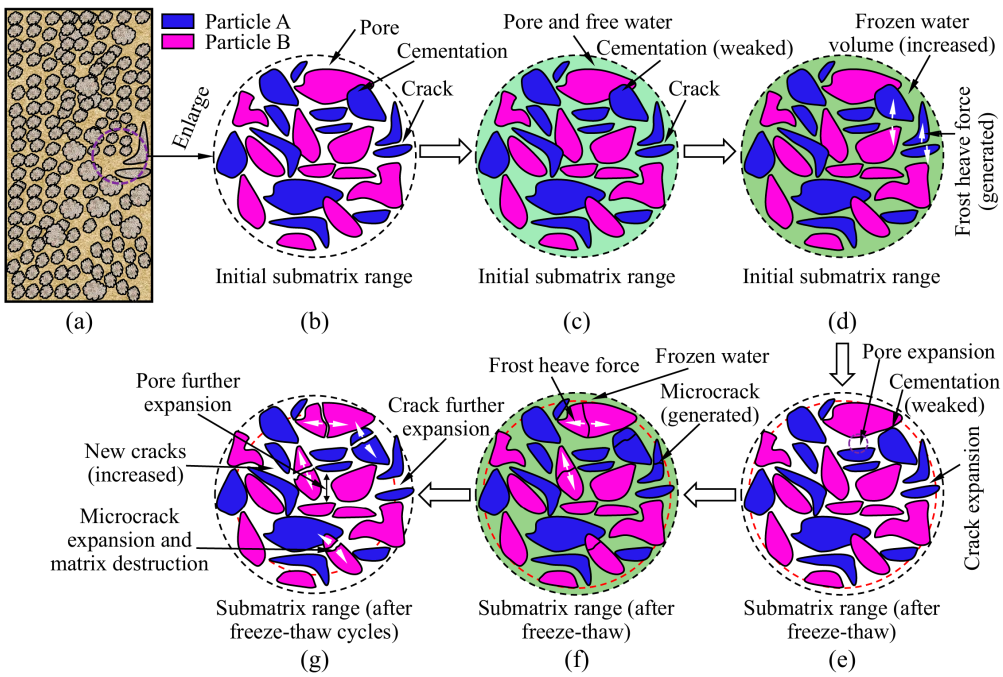


**Figure 16.** The evolution process of the internal structure of fine-grained sandstone samples from the Yan'an Formation in the Tarangole coal mining area under freeze–thaw conditions. (**a**) Fine- grained sandstone standard sample; (**b**) natural state; (**c**) saturated state; (**d**) the first freeze stage; (**e**) the first thaw stage; (**f**) repeated freezing; and (**g**) multiple freeze–thaw cycles.

Firstly, in the natural state, fine-grained sandstone consists of various matrix particles cemented together and contains primary pores and fractures (Figure 16b). After saturation treatment, water fills the pores and cracks and adheres to the particle surfaces, thereby reducing interparticle friction. Meanwhile, free water dissolves soluble minerals, weakens cementation, and slightly reduces resistance to deformation (Figure 16c). When the rock sample transitions from the saturated stage (Figure 16c) to the first freeze stage (Figure 16d), the free water within the pores and cracks freezes and expands. This freeze-induced expansion exerts a compressive force on the surrounding matrix, causing it to deform. Meanwhile, tensile stresses concentrate at the crack tips, leading to initial freezing damage. Additionally, during the cooling process, the submatrix particles contract. Due to differences in their coefficients of thermal expansion, this contraction is uneven, further weakening the bond between the particles. When the rock sample enters the first thaw stage (Figure 16e), its temperature rises, and the ice crystals melt into free water, which then migrates into the newly formed pores and cracks. After multiple freeze–thaw cycles, primary pores and cracks further expand, secondary and through-going cracks increase, resistance to deformation weakens, strength decreases, and mechanical properties transition from brittle to ductile. The failure mode evolves from shear failure to shear-tension composite failure (Figure 16g).

Moreover, as the temperature drops, the matrix particles contract more significantly. The difference in thermal expansion coefficients between the phases leads to increased relative displacement between the particles, thereby further weakening interfacial bonding. Therefore, at low temperatures, secondary and through cracks inside the samples increase in number and become unevenly distributed, resulting in more severe damage. Meanwhile, the distribution of macroscopic tensile and shear cracks on the surface becomes denser.

## 5. Discussion

### *5.1. Constitutive Model and Damage Equation for Sandstone Under Freeze–Thaw Cycles*

#### 5.1.1. Establishment of Damage Models

The progressive failure of sandstone under external loading is essentially a process of cumulative damage. In this study, the degree of damage is determined not only by axial stress and confining pressure, but also by the internal structural changes induced by freeze–thaw cycles [55]. Most of the currently used rock damage models are based on the Lemaitre strain equivalence principle, which assumes that the post-peak residual strength of rocks is zero after failure. However, this assumption is clearly inconsistent with the results of triaxial compression tests [56]. For this reason, some scholars have proposed corrections and developed a local damage model capable of describing the residual strength after the peak load, and the corresponding loading configuration is illustrated in Figure 17.

This model divides rock materials into undamaged and damaged zones and assumes that damage occurs only in the direction normal to the cross-section of the sample during loading. Suppose the cross-sectional areas of the undamaged and damaged zones are $S'$ and $S''$, respectively, and the total area is $S$. Then the damage variable $D$ is defined as follows.

$$D = \frac{S'}{S} \tag{1}$$

Since rock damage occurs only on cross-sections whose normal is aligned with the axial direction, the apparent stress and strain in all directions must satisfy the following relationship.

$$\sigma_1 = \sigma_1'(1 - D) + \sigma_1'' D \tag{2}$$

$$\varepsilon_1 = \varepsilon_1' = \varepsilon_1'' \tag{3}$$

$$\sigma_2 = \sigma_2' = \sigma_2'' \tag{4}$$

$$\sigma_3 = \sigma_3' = \sigma_3'' \tag{5}$$

where $\sigma_i$ ($i$ = 1, 2, 3) represents the apparent stress applied to the sandstone in three orthogonal directions; $\sigma_i{}'$ and $\sigma_i{}''$ denote the stresses in the undamaged and damaged parts of the material, respectively, MPa; and $\varepsilon_1$ is the apparent axial strain of the rock, while $\varepsilon_1{}'$ and $\varepsilon_1{}''$ are the corresponding apparent axial strains in the undamaged and damaged parts, respectively.

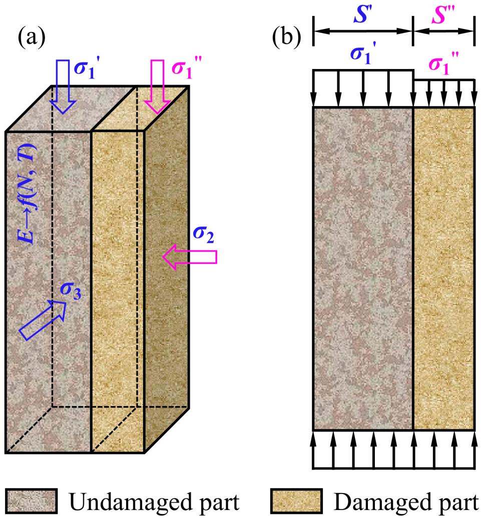


**Figure 17.** Schematic diagram of the force-induced damage model for sandstone. (**a**) 3D force application; and (**b**) planar perspective.

Assuming that the undamaged part of the rock undergoes only elastic deformation, it obeys the generalized Hooke's law [57]. At this point, the stress–strain relationship for the undamaged part is defined as follows.

$$\sigma_1' = E\varepsilon_1' + v(\sigma_2' + \sigma_3') \tag{6}$$

where $v$ is Poisson's ratio; $E$ is the elastic modulus, GPa, and its value is closely related to the number of freeze–thaw cycles, the freezing temperature, and the confining pressure level.

According to Sections 4.1.2 and 4.2.2, the relationship surface diagrams for ($N$, $T$) under uniaxial compression and for ($N$, $\sigma_3$) under triaxial compression, respectively, are shown in Figure 18.

The nonlinear surface fitting was performed using Origin software (Version 2018), and the general expressions for the two surfaces were obtained as follows.

$$E_{f(N,T)} = E_0(A_1N^2 + A_2T^2 + A_3NT + A_4N + A_5T + A_6),\ R^2 = 0.98 \tag{7}$$

$$E_{f(N,\sigma_3)} = E_1(A_1N^2 + A_2\sigma_3{}^2 + A_3N\sigma_3 + A_4N + A_5\sigma_3 + A_6),\ R^2 = 0.99 \tag{8}$$

where $E_{f(N,T)}$ represents the elastic modulus of the rock sample under any freeze–thaw condition, GPa; $E_0$ and $E_1$ represent the initial elastic moduli of the sample under uniaxial compression at $N$ = 5, $T$ = −5 °C and at $N$ = 0, $T$ = 20 °C, respectively, GPa; and $A_j$ ($j$ = 1, 2, 3, 4, 5, 6) is the coefficient of the surface-fitting function, and its specific values are listed in Table 2.

To analyze the weakening pattern of slope stability under freeze–thaw temperature variations and freeze–thaw cyclic conditions, a strength degradation equation can be fitted and incorporated into the strength reduction method to calculate the safety factor at different freeze–thaw stages [58].

**Table 2.** Coefficients of the surface-fitting function.

| Equation | Variable | $A_1$ | $A_2$ | $A_3$ | $A_4$ | $A_5$ | $A_6$ |
|---|---|---|---|---|---|---|---|
| (7) | $(N,T)$ | $8.2 \times 10^{-4}$ | $4.9 \times 10^{-4}$ | $-2.3$ | $-4.3 \times 10^{-2}$ | $-2.3 \times 10^{-2}$ | 1.3 |
| (8) | $(N,\sigma_3)$ | $1.4 \times 10^{-3}$ | $-3.8 \times 10^{-2}$ | $-2.4 \times 10^{-2}$ | $-5.3 \times 10^{-2}$ | 0.94 | 1.1 |

Furthermore, if the axial stress of the damaged part of the rock is taken as the post-peak residual strength, denoted by $\sigma_R$, then the stress in this region satisfies the following relationship.

$$\sigma_i'' = \sigma_R \quad (9)$$

Finally, substituting Equations (3)–(9) into Equation (2) sequentially and organizing the results yields the axial stress-damage constitutive equation that accounts for the effects of freeze–thaw cycles and freezing temperature, expressed as follows.

$$\sigma_1 = (1 - D)[E_{f(N,T)}\varepsilon_1 + v(\sigma_2 + \sigma_3)] + D\sigma_R \quad (10)$$

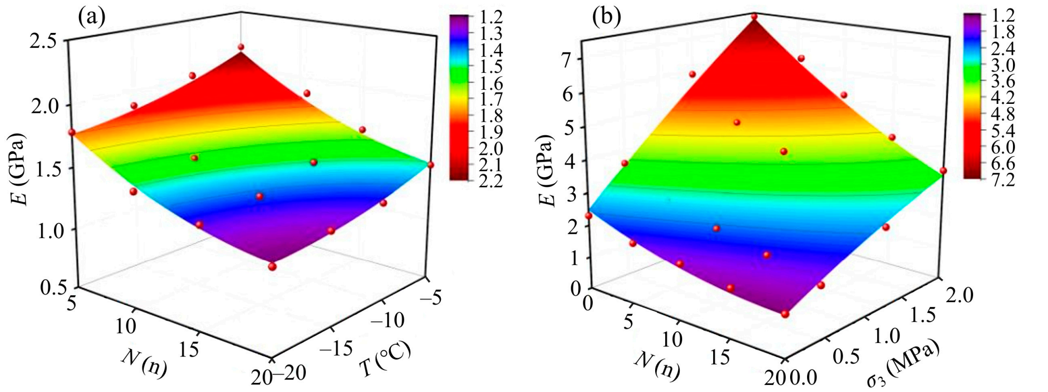


**Figure 18.** Surface plots illustrating the relationships among $(N, T)$, $(N, \sigma_3)$, and $E$. (**a**) The relationship between $(N, T)$ and $E$; and (**b**) the relationship between $(N, \sigma_3)$ and $E$.

### 5.1.2. Evolution Equation for Damage

(1) Establishment of a Statistical Damage Equation

In Section 4, under freeze–thaw cycles and varying freezing temperatures, the uniaxial compressive stress–strain curves of fine-grained sandstone from the Yan'an Formation in the Tarangole coal mine all exhibit a post-peak brittle drop followed by fluctuating ductile behavior, with a residual strength of zero. During triaxial compression, some samples exhibited an immediate stress drop after reaching the peak strength, whereas others showed a gradual decline. All samples retained residual strength after failure. To describe the characteristics of the aforementioned post-peak stress–strain curves, a microelement strength distribution function capable of capturing the softening behavior should be selected to establish an applicable damage evolution equation.

In this study, the Weibull distribution was modified by incorporating a correction factor $Q$ to better describe diverse post-peak stress–strain drop characteristics [59]. The corrected cumulative distribution function and the corresponding differential (elemental) strength distribution function are given below.

$$D = 1 - Qexp[-(\frac{F}{F_0})^n] = 1 - exp[-(\frac{F}{F_0})^{kn}] \times exp[-(\frac{F}{F_0})^n] \quad (11)$$

$$p(F)=\frac{\partial D}{\partial F}=\frac{n}{F_0}(\frac{F}{F_0})^{n-1}[1+k(\frac{F}{F_0})^{(k-1)n}]\times exp\left\{-(\frac{F}{F_0})^{n}[1+(\frac{F}{F_0})^{(k-1)n}]\right\} \tag{12}$$

where $F_0$ and $n$ are the proportionality parameter and shape parameter, respectively; $k$ is the post-peak shape correction coefficient of the stress–strain curve; and $F$ is the strength of the infinitesimal element.

Since the rock is divided into undamaged and damaged parts, and the damaged part has entered the post-peak softening (or post-peak strain-softening) regime, the micro-element strength $F$ is defined only for the undamaged part. Assuming that rock failure obeys the Mohr-Coulomb yield criterion, the expression for $F$ is as follows.

$$F=(1-sin\varphi_{NT})\sigma_1'-(1+sin\varphi_{NT})\sigma_3' \tag{13}$$

where $\varphi_{NT}$ represents the internal friction angle of the rock under specific freeze–thaw cycles and freezing temperature, °.

Substituting Equations (3)–(8) into Equation (13) and simplifying, the differential intensity $F$ is obtained as follows.

$$F=(1-sin\varphi_{NT})[E_{f(N,T)}\varepsilon_1+v(\sigma_2+\sigma_3)]-(1+sin\varphi_{NT})\sigma_3 \tag{14}$$

By substituting Equations (11) and (14) into Equation (10), the specific expression of the axial stress-damage constitutive equation for rock samples subjected to varying numbers of freeze–thaw cycles and different freezing temperatures was obtained.

$$\begin{aligned}\sigma_1 \;=\; & exp[-(\tfrac{(1-sin\varphi_{NT})[E_{f(N,T)}\varepsilon_1+v(\sigma_2+\sigma_3)]-(1+sin\varphi_{NT})\sigma_3}{F_0})^{kn}] \\ & \times exp[-(\tfrac{(1-sin\varphi_{NT})[E_{f(N,T)}\varepsilon_1+v(\sigma_2+\sigma_3)]-(1+sin\varphi_{NT})\sigma_3}{F_0})^{n}] \\ & \times [E_{f(N,T)}\varepsilon_1+v(\sigma_2+\sigma_3)]+[1 \\ & -exp[-(\tfrac{(1-sin\varphi_{NT})[E_{f(N,T)}\varepsilon_1+v(\sigma_2+\sigma_3)]-(1+sin\varphi_{NT})\sigma_3}{F_0})^{kn}] \\ & \times exp[-(\tfrac{(1-sin\varphi_{NT})[E_{f(N,T)}\varepsilon_1+v(\sigma_2+\sigma_3)]-(1+sin\varphi_{NT})\sigma_3}{F_0})^{n}]] \\ & \times \sigma_R\end{aligned} \tag{15}$$

(2) Solution of the damage equation parameters

From Equation (15), it can be seen that to obtain the specific expressions for the damage evolution equation and the axial stress-damage constitutive equation, it is first necessary to determine the proportionality parameter $F_0$, the shape parameter $n$, and the post-peak shape parameter $k$. Suppose the peak stress and peak strain at the peak point of the stress–strain curve of the sample are $\sigma_{1max}$ and $\varepsilon_{1max}$, respectively; then, by solving the simultaneous Equations (10) and (11), we can obtain the corresponding parameters.

$$\begin{aligned} & D_{\varepsilon_1=\varepsilon_{1max}}=1-exp\{-(\tfrac{F_{max}}{F_0})^{n}[1+(\tfrac{F_{max}}{F_0})^{(k-1)n}]\} \\ & =\tfrac{\sigma_{1max}-E_{f(N,T)}\varepsilon_1+v(\sigma_2+\sigma_3)\varepsilon_{1max}-v(\sigma_2+\sigma_3)}{\sigma_R-E_{f(N,T)}\varepsilon_1+v(\sigma_2+\sigma_3)\varepsilon_{1max}-v(\sigma_2+\sigma_3)}\end{aligned} \tag{16}$$

where $F_{max}=(1-sin\varphi_{NT})\sigma_{1max}-(1+sin\varphi_{NT})\sigma_3$.

When the axial stress–strain curve of the sample reaches its peak point, the slope of the curve at that point is zero. Differentiating Equation (10) yields this result.

$$(1-D)E_{f(N,T)}+[\sigma_R-v(\sigma_2+\sigma_3)-E_{f(N,T)}\varepsilon_1]\frac{\partial D}{\partial\varepsilon_1},\ \varepsilon_1=\varepsilon_{1max} \tag{17}$$

Substituting Equation (11) into Equation (17) yields the following result.

$$1 = \frac{n}{F_0}\left(\frac{F_{max}}{F_0}\right)^{n-1}\left[1 + k\left(\frac{F_{max}}{F_0}\right)^{(k-1)n}\right] \times [E_{f(N,T)}\varepsilon_{1max} + v(\sigma_2 + \sigma_3) - \sigma_R](1 - sin\varphi_{NT}) \quad (18)$$

Therefore, by simultaneously solving Equations (16) and (18), the damage equation and the axial stress-damage constitutive equation for fine-grained sandstone from the Yan'an Formation in the Tarangole coal mine under varying freeze–thaw cycles and freezing temperatures can be obtained.

5.1.3. Constitutive Model Accuracy Verification

To verify the constitutive model's accuracy, stress–strain curves obtained under different confining pressures after 5 and 20 freeze–thaw cycles were selected for parameter fitting and validation. Table 3 shows the initial model parameters and the corresponding relative calculation error. Figure 19 depicts the comparison between the experimental and theoretical results.

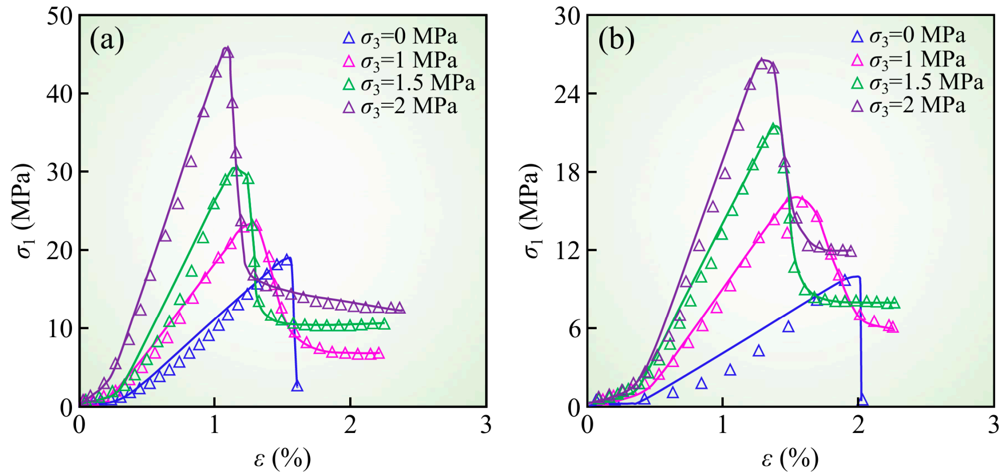


**Figure 19.** Comparison between the results of physical tests and those of theoretical model calculations. (**a**) $N$ = 5, $T$ = −5 °C; and (**b**) $N$ = 20, $T$ = −5 °C.

**Table 3.** The initial parameter settings of the theoretical model and the relative error of the calculation results.

| $N$ (n) | $T$ (°C) | $\sigma_3$ (MPa) | $E$ (GPa) | $v$ | $F_0$ | $n$ | $k$ | Error of $\sigma_R$ (%) |
|---|---|---|---|---|---|---|---|---|
| 5 | −5 | 1 | 2.88 | 0.2 | 8.5 | 3.2 | 3 | 4.6 |
| | | 1.5 | 4.59 | 0.2 | 19.1 | 2.4 | 3 | 6.9 |
| | | 2 | 6.07 | 0.2 | 32.1 | 1.6 | 3 | 5.7 |
| 20 | −5 | 1 | 1.77 | 0.23 | 9.5 | 4.6 | 3 | 6.4 |
| | | 1.5 | 2.72 | 0.23 | 18.8 | 6.2 | 3 | 3.6 |
| | | 2 | 3.36 | 0.23 | 30.3 | 3.4 | 3 | 4.1 |

Figure 19 and Table 3 demonstrate that the stress–strain curves obtained using the axial stress-damage constitutive equation established in this subsection are generally consistent with the test results, although the fitting error in the pre-peak region is slightly larger than that in the post-peak region. Nevertheless, the residual strength error after the peak is controlled within 7%, satisfying the model requirements. Therefore, the damage constitutive model proposed in this study—which accounts for both the number of freeze–thaw cycles and the freezing temperature—can effectively describe the entire damage and failure process of fine-grained sandstone from the Yan'an Formation in the Tarangole coal mine under various loading conditions. In addition, this model can accurately capture its characteristic behaviors, such as brittle fracture, strain softening, and residual strength.

The theoretical foundation of the constitutive model for damage in fine-grained sandstone under freeze–thaw conditions is statistical damage mechanics, which assumes that the strength of microelements follows a Weibull distribution to reflect the rock’s heterogeneity and the strength degradation induced by freeze–thaw cycles. This distribution can reasonably represent the random variation in microelement strength after freeze–thaw cycles, thereby facilitating the establishment of a quantitative relationship among the number of freeze–thaw cycles, temperature, and mechanical parameters. Additionally, the modeling process follows the principles of segmented coupling, multi-factor and multi-scale coupling, experiment-driven development, and parameter calibration.

### 5.2. Engineering Initiatives and Prospects

In view of the freeze–thaw environment affecting the soft-to-moderately-soft sandstone at the Tarangole coal mine, the influence of freeze–thaw cycles on long-term slope stability must be systematically evaluated. The following relevant suggestions are offered: on the one hand, when designing support structures (e.g., anchor rods and anti-slide piles), due consideration should be given to the reduction in rock mass strength and the frost-heave force induced by freeze–thaw cycling. Thus, safety redundancy should be appropriately increased. On the other hand, research shows that low-temperature freezing can effectively enhance the strength of saturated sandstone, a finding that can inform the optimization of winter construction plans. Meanwhile, during cold seasons, it is necessary to ensure that the interception and drainage system remains functional despite freezing conditions (e.g., by using underground drainage pipes or implementing insulation measures) and to closely monitor the slope’s dynamic response during the spring thaw period. Moreover, in international research, the method combining numerical simulation with indoor mechanical testing can be adopted to obtain more accurate strength characteristics and mechanical parameters of both loose rock masses and hard or semi-hard rocks, thereby improving the stability assessment of slopes and rock walls in the study area [60].

The innovation of this study lies primarily in investigating the mechanical properties of fine-grained sandstone from the Tarangole coal mining area under varying freeze–thaw cycles and freezing temperatures through mechanical testing—providing theoretical guidance for slope stability and surface subsidence assessment in the study area. The deficiency lies in the fact that intelligent or numerical techniques have not been used to compare and verify the experimental data. In the future, we will continue to integrate numerical simulation and machine learning techniques to investigate the mechanical properties of sandstone and slope stability in the Tarangole coal mining area. Moreover, we will investigate the mechanical properties of other rock types in the Tarangole coal mine area by determining parameters such as the internal friction angle and cohesion under various freeze–thaw cycles and temperature conditions through laboratory tests, thereby enabling a more reliable assessment of slope stability.

## 6. Conclusions

In this study, fine-grained sandstone from the Yan’an Formation in the Tarangole mining area is selected as the research subject. Laboratory mechanical tests are conducted under varying freeze–thaw cycles, freezing temperatures, and confining pressures to systematically investigate the evolution of freeze–thaw damage, deformation and failure characteristics, and mesoscale deterioration mechanisms in sandstone. Based on these, a damage constitutive model incorporating freeze–thaw effects is established. The main conclusions are as follows:

(1) Freeze–thaw cycles and freezing temperature critically control the mechanical deterioration of sandstone. Both the elastic modulus and the peak strength decrease exponentially with an increasing number of cycles or with decreasing temperature. Furthermore, freeze–thaw cycles dominate the reduction in elastic modulus (≈12% per 5 cycles), whereas peak strength is most sensitive to temperature in the −5 °C to −15 °C range and to cycling during the first 10 cycles. In addition, peak strain increases quasi-exponentially with increasing cycle number and decreasing temperature; the coupling of low-temperature and high-cycle loading promotes plastic deformation.
(2) Confining pressure inhibits freeze–thaw damage in sandstone, but this inhibitory effect weakens significantly after 10 freeze–thaw cycles. Under different cycles, the elastic modulus and peak strength increase approximately linearly with confining pressure, while peak strain decreases, indicating improved bearing capacity and deformation resistance. Beyond 10 cycles, internal damage in sandstone intensifies, the load-bearing capacity of the skeleton particles declines, and the rock mass becomes significantly less sensitive to increases in confining pressure.
(3) Freeze–thaw cycles progressively deteriorate the pore–crack structure and particle cementation of sandstone, thereby altering its macroscopic failure behavior. Furthermore, under uniaxial compression, sandstone transitions from single or conjugate shear failure to shear-tension composite failure as the number of freeze–thaw cycles increases and the freezing temperature decreases. Mesoscopically, frost heave driven by water-ice phase transition and differential thermal expansion degrades interparticle bonding, promotes crack propagation and pore expansion, and thus continuously weakens the mechanical properties of sandstone.
(4) Based on damage mechanics and the modified Weibull distribution, a constitutive model for sandstone is developed to account for the effects of freeze–thaw cycles, freezing temperature, and confining pressure. Here, the model agrees well with test data (post-peak residual strength error < 7%) and captures the full stress–strain response under freeze–thaw cycling, including brittle fracture, strain softening, and residual strength.

**Author Contributions:** Conceptualization, J.L., Z.L. and S.W.; methodology, S.W.; software, S.W.; validation, J.L., S.W. and Y.L.; formal analysis, Z.L. and X.T.; investigation, J.L.; resources, Z.L.; data curation, Z.L., Y.L. and X.T.; writing—original draft preparation, J.L.; writing—review and editing, S.W. and Y.L.; visualization, J.L. and Z.L.; supervision, Y.L.; project administration, J.L.; funding acquisition, J.L. All authors have read and agreed to the published version of the manuscript.

**Funding:** This research received no external funding.

**Institutional Review Board Statement:** Not applicable.

**Informed Consent Statement:** Not applicable.

**Data Availability Statement:** Most of the data generated during this study are included in the article. For other datasets, please contact the corresponding author with reasonable requests.

**Conflicts of Interest:** Author Jianhua Li was employed by China Energy Group Hangjin Energy Company Ordos. Author Zhibin Li was employed by CCTEG Xi'an Research Institute (Group) Co., Ltd.. The remaining authors declare that the research was conducted in the absence of any commercial or financial relationships that could be construed as a potential conflict of interest.

## References

1. Li, Q.; Chen, H.; Long, R.Y.; Huang, Z.P. Who is leading the methanol price? The roles of international transmission and energy price based on the PLBX model. *Energy* **2026**, *346*, 140145. [CrossRef]

2. Kennedy, C.; Zhong, M.; Corfee-Morlot, J. Infrastructure for China's Ecologically Balanced Civilization. *Engineering* **2016**, *2*, 414–425. [CrossRef]
3. Wang, Y.R.; Li, J.J.; Zhang, J.; Yan, Y.L.; Zhang, S.; Li, Z.; Li, M.G.; Peng, L.; Xie, K.C. Water footprint of China's coal mining sector substantially underestimated. *Ecol. Indic.* **2025**, *180*, 114310. [CrossRef]
4. Wang, Z.M.; Yan, J.L.; Zhou, W.; Luo, H.T. WRF-FLUENT coupled modeling approach for simulating airflow and dust dispersion during cold periods in cold-region open-pit mines. *J. Hazard. Mater.* **2026**, *503*, 141242. [CrossRef] [PubMed]
5. Guo, Z.Q.; Liu, G.W.; Chai, S.L.; Liu, W.; Jiang, F. Implementation and intelligent path exploration of multimodal large model architecture for open-pit coal mine production. *Results Eng.* **2026**, *29*, 109283. [CrossRef]
6. Rezaei, M.; Mousavi, S.Z.S. Slope stability analysis of an open pit mine with considering the weathering agent: Field, laboratory and numerical studies. *Eng. Geol.* **2024**, *333*, 107503. [CrossRef]
7. Li, Q.H.; Wang, Y.M.; Li, X.S.; Tang, S.B.; Gong, B.; Jiang, S. Evolutionary characteristics of the fracture network in rock slopes under the combined influence of rainfall and excavation. *Bull. Eng. Geol. Environ.* **2025**, *84*, 47. [CrossRef]
8. Li, X.S.; Li, Q.H.; Wang, Y.M.; Liu, W.; Hou, D.; Zhu, C. Effect of slope angle on fractured rock masses under combined influence of variable rainfall infiltration and excavation unloading. *J. Rock Mech. Geotech. Eng.* **2024**, *16*, 4154–4176. [CrossRef]
9. Li, B.W.; Liu, R.T.; Qiu, Q.Y.; Zhang, H.Q.; Rong, G. Experimental study on mechanical behavior of basalt under different freeze-thaw conditions. *Bull. Eng. Geol. Environ.* **2025**, *84*, 222. [CrossRef]
10. Park, J.; Hyun, C.U.; Park, H.D. Changes in microstructure and physical properties of rocks caused by artificial freeze-thaw action. *Bull. Eng. Geol. Environ.* **2015**, *74*, 555–565. [CrossRef]
11. Letshwiti, T.M.; Shahsavar, M.; Moniri-Morad, A.; Sattarvand, J. Deep learning-based image segmentation for highwall stability monitoring in open pit mines. *J. Eng. Res.* **2025**, *13*, 3595–3608. [CrossRef]
12. Zhang, N.B.; Wang, Y.J.; Zhao, F.; Wang, T.; Zhang, K.W.; Fan, H.D.; Zhou, D.W.; Zhang, L.X.; Yan, S.Y.; Diao, X.P.; et al. Monitoring and Analysis of the Collapse at Xinjing Open-Pit Mine, Inner Mongolia, China, Using Multi-Source Remote Sensing. *Remote Sens.* **2024**, *16*, 993. [CrossRef]
13. Büyükakpnar, P.; Carrillo-Ponce, A.C.; Munir, M.B.; Karasözen, E.; Tanyas, H.; Ertuncay, D.; Palliath, A.; Gorum, T. Seismic, Field, and Remote Sensing Analysis of the 13 February 2024 Çöpler Gold Mine Landslide, Erzincan, Türkiye. *Seism. Rec.* **2025**, *5*, 165–174. [CrossRef]
14. Ma, Q.; Liu, X.L.; Tan, Y.L.; Wang, R.S.; Xie, W.Q.; Wang, E.Z.; Liu, X.S.; Shang, J.L. Experimental Study of Loading System Stiffness Effects on Mechanical Characteristics and Kinetic Energy Calculation of Coal Specimens. *Rock Mech. Rock Eng.* **2024**, *57*, 9941–9957. [CrossRef]
15. Peng, Z.X.; Qu, J.H.; Chen, C.Q.; Wang, H.H.; Zhu, D.C.; Mi, Z.R.; Xie, E.; Zhang, Z.H.; Yu, X.H.; Wang, H. Coal Accumulation in Marine to Continental Transitional Sequence During Late Carboniferous-Early Permian in the Southeastern Ordos Basin, China. *Geol. J.* **2026**, *61*, 549–565. [CrossRef]
16. Li, Z.B.; Liu, N.; Li, J.H.; Wang, S.C.; Luo, Y.J.; Tan, X.J. Experimental Study on the Frozen Creep Mechanics of Sandstone in the Tarangole Coal Mining Area. *Appl. Sci.* **2026**, *16*, 2725. [CrossRef]
17. Hu, S.H.; Hu, Y.J.; Xu, H.Y.; Ai, D.; Yuan, J.J.; Kou, L.; Huang, W.; Zhou, C. Failure Mechanism of the Yizhuxiang Collapse under the Joint Effect of Freeze-Thaw and Mining. *Appl. Sci.* **2023**, *13*, 3801. [CrossRef]
18. Li, J.H.; Li, H.J.; Li, W.; Li, L.; Jiang, P.; Du, M.Z. Water inrush mechanism and prevention for thick coal mining under an extremely thick glutenite layer: A case study in the southwest of the Ordos Basin. *Bull. Eng. Geol. Environ.* **2023**, *82*, 389. [CrossRef]
19. Azhari, A.; Ozbay, U. Investigating the effect of earthquakes on open pit mine slopes. *Int. J. Rock Mech. Min.* **2017**, *100*, 218–228. [CrossRef]
20. Li, Q.H.; Song, D.Q.; Yuan, C.M.; Nie, W. An image recognition method for the deformation area of open-pit rock slopes under variable rainfall. *Measurement* **2022**, *188*, 110544. [CrossRef]
21. Li, X.S.; Li, Q.H.; Wang, Y.M.; Liu, W.; Hou, D.; Zheng, W.B.; Zhang, X. Experimental study on instability mechanism and critical intensity of rainfall of high-steep rock slopes under unsaturated conditions. *Int. J. Min. Sci. Technol.* **2023**, *33*, 1243–1260. [CrossRef]
22. Zheng, P.C.; Tan, X.J.; Du, Z.H.; Liu, X.H.; Zhou, Y.; Shen, K.; Guan, B.; Chen, W.Z. Microscopic damage and deterioration of carbonaceous slate in cold region subjected to freeze-thaw cycles. *J. Rock Mech. Geotech. Eng.* **2026**, *18*, 113–128. [CrossRef]
23. Wang, Y.; Liu, F.; Kou, M.M.; Li, M.F. A Review of Stability of Dam Structures in Coal Mine Underground Reservoirs. *Water* **2024**, *16*, 1856. [CrossRef]
24. Wang, J.G.; Yang, S.; Ren, L.R.; Wei, Z.G.; Cong, Y.R. Characteristics and modeling of shale creep under osmotic pressure: Innovations with fractional Calculus and strain energy-based methods. *Bull. Eng. Geol. Environ.* **2025**, *84*, 536. [CrossRef]
25. Khanlari, G.; Abdilor, Y. Influence of wet-dry, freeze-thaw, and heat-cool cycles on the physical and mechanical properties of Upper Red sandstones in central Iran. *Bull. Eng. Geol. Environ.* **2015**, *74*, 1287–1300. [CrossRef]
26. Yang, C.; Zhou, K.P.; Xiong, X.; Deng, H.W.; Pan, Z. Experimental investigation on rock mechanical properties and infrared radiation characteristics with freeze-thaw cycle treatment. *Cold Reg. Sci. Technol.* **2021**, *183*, 103232. [CrossRef]

27. Zhang, X.L.; Liu, X.L.; Jin, J.X.; Wang, H.B.; Lv, Z.Q.; Xiao, Y. Investigation of damage characteristics in freeze-thawed grey-white sandstone using AE multifractal analysis. *Geomech. Geophys. Geo-Energy Geo-Resour.* **2025**, *11*, 93. [CrossRef]
28. Yahaghi, J.; Liu, H.Y.; Chan, A.; Fukuda, D. Experimental and numerical studies on failure behaviours of sandstones subject to freeze-thaw cycles. *Transp. Geotech.* **2021**, *31*, 100655. [CrossRef]
29. Yin, T.B.; Lu, J.F.; Yu, Y.; Wu, Y.; Wang, J.H.; Men, J.Q. Fracture behavior of yellow sandstone under freeze-thaw cycles with varied saturation states: An investigation of mode I fracture. *Geomech. Energy Environ.* **2023**, *36*, 100502. [CrossRef]
30. Xu, Y.; Fu, Y.; Yang, Y.X.; Yao, W.; Xia, K.W.; Peng, J.B. Dynamic compression properties of a saturated white sandstone under ambient sub-zero temperatures. *Acta Geotech.* **2023**, *18*, 4245–4260. [CrossRef]
31. Korkanç, M.; Hüseyinca, M.Y.; Hatir, M.E.; Tosunlar, M.B.; Bozdag, A.; Özen, L.; Ince, I. Interpreting sulfated crusts on natural building stones using sulfur contour maps and infrared thermography. *Environ. Earth Sci.* **2019**, *78*, 378. [CrossRef]
32. Feng, Q.; Jin, J.C.; Zhang, S.; Liu, W.W.; Yang, X.X.; Li, W.T. Study on a Damage Model and Uniaxial Compression Simulation Method of Frozen-Thawed Rock. *Rock Mech. Rock Eng.* **2022**, *55*, 187–211. [CrossRef]
33. Zhou, Y.F.; Huang, H.Y.; Liu, M.; Li, M.Y.; Suo, X.Q. Frost heave model and frost heaving force analysis of permafrost tunnel based on segregated ice. *Tunn. Undergr. Space Technol.* **2024**, *147*, 105715. [CrossRef]
34. Yang, Z.Y.; Xu, Y.; Yu, M.L.; Li, C.J.; Li, Y.F.; Yang, R.Z.; Zheng, Q.Q. Failure mechanism of unsaturated sandstone under freeze-thaw cycles: Critical saturation effect and segmented damage modeling. *Eng. Fract. Mech.* **2026**, *335*, 111902. [CrossRef]
35. Li, T.; Tang, J.T.; Liu, W.L.; Sun, X.N.; Wang, H.Y.; Lu, G.Y. Research on Freeze-Thaw Cycle Rock Damage Combining Multiscale Simulation and Test Validation. *Int. J. Geomech.* **2025**, *25*, 04025198. [CrossRef]
36. Lv, Z.T.; Yan, M.X.; Wu, M.C.; Xia, C.C.; Liu, W.P. Freeze-thaw deformation characteristics and thermo-mechanical coupled freeze-thaw deformation model of unsaturated rocks. *Eng. Geol.* **2025**, *359*, 108441. [CrossRef]
37. Yahaghi, J.; Liu, H.Y.; Chan, A.D.; Fukuda, D. Experimental, theoretical and numerical modelling of the deterioration and failure process of sandstones subject to freeze-thaw cycles. *Eng. Fail. Anal.* **2022**, *141*, 106686. [CrossRef]
38. Li, K.P.; Li, Y.; Yin, F.T.; Dai, F.; Wang, C.; Zhang, S.W.; Wang, K. Mechanical properties and failure mechanism of rock-like specimens with arc-shaped flaws under freeze-thaw cycles. *Theor. Appl. Fract. Mech.* **2024**, *130*, 104275. [CrossRef]
39. Zhang, X.; Liu, Z.G.; Chang, S.; Xue, Y.L.; Zhang, J.Y. Study on damage characteristics and fracture mechanisms of coal under high stress environment during blasting. *Eng. Fract. Mech.* **2025**, *314*, 110772. [CrossRef]
40. Kahraman, E.; Ozdemir, A.C. The prediction of durability to freeze-thaw of limestone aggregates using machine-learning techniques. *Constr. Build Mater.* **2022**, *324*, 126678. [CrossRef]
41. Zhong, W.; Yuan, Q.Q.; Liu, T.T.; Yue, L.W. Freeze/thaw onset detection combining SMAP and ASCAT data over Alaska: A machine learning approach. *J. Hydrol.* **2022**, *605*, 127354. [CrossRef]
42. Li, X.; Zhang, K.; Niu, J.F.; Liu, L.X. A machine learning-based dynamic ensemble selection algorithm for microwave retrieval of surface soil freeze/thaw: A case study across China. *GIScience Remote Sens.* **2022**, *59*, 1550–1569. [CrossRef]
43. Johnson, J.I.; Sharman, G.R.; Szymanski, E.; Huang, X. Machine Learning Applied to a Modern-Pleistocene Petrographic Data Set: The Global Prediction of Sand Modal Composition (GloPrSM) Model. *J. Geophys. Res.-Earth* **2022**, *127*, e2022JF006595. [CrossRef]
44. Zhou, S.T.; Zhang, Z.X.; Luo, X.D.; Huang, Y.F.; Yu, Z.; Yang, X.W. Predicting dynamic compressive strength of frozen-thawed rocks by characteristic impedance and data-driven methods. *J. Rock Mech. Geotech. Eng.* **2024**, *16*, 2591–2606. [CrossRef]
45. Lu, J.; Peng, X.; Yin, L.S.; Ling, Z.Y.; Yang, M.F.; Zhang, P.X.; Zhou, K.; Liu, L.; Dai, S.F.; Shao, L.Y.; et al. Influence of plant terrestrialization on coal accumulation and deep time terrestrial carbon storage. *Earth-Sci. Rev.* **2026**, *274*, 105390. [CrossRef]
46. Lu, X.; Tu, L.X.; Tian, Y.; Zhou, W.; Zhao, X.J.; Yang, Y.Q. Experimental Study of the Freeze–Thaw Damage of Alpine Surface Coal Mine Roads Based on Geopolymer Materials. *Water* **2023**, *15*, 3903. [CrossRef]
47. Ciais, P.; Tagliabue, A.; Cuntz, M.; Bopp, L.; Scholze, M.; Hoffmann, G.; Lourantou, A.; Harrison, S.P.; Prentice, I.C.; Kelley, D.I.; et al. Large inert carbon pool in the terrestrial biosphere during the Last Glacial Maximum. *Nat. Geosci.* **2012**, *5*, 74–79. [CrossRef]
48. Shen, F.Q.; Qiu, W.L.; Xie, K.; Xing, M.M.; Zhu, H.W.; Huang, S.B. A discrete element-based study of freeze-thaw damage in water-filled fractured rock. *Comput. Geotech.* **2025**, *185*, 107343. [CrossRef]
49. Zhang, M.Z.; Song, Y.; Li, C.H.; Zhao, Y.L.; Tang, J.Z.; Li, K.S. Experimental investigation on fatigue mechanical behavior and energy evolution characteristic of fine-grained marble under multilevel constant-amplitude cyclic loading. *Rock Mech. Bull.* **2026**, *5*, 100269. [CrossRef]
50. Lu, H.Q.; Bao, W.X.; Yin, Y.; Sun, X.; Li, H.Z.; Pan, Z.H.; Che, B.W. Experimental study on multi-scale damage and deterioration mechanism of carbonaceous slate under freeze-thaw cycles. *Bull. Eng. Geol. Environ.* **2023**, *82*, 458. [CrossRef]
51. Zhang, L.; Wang, G.L.; Liu, B.L.; Sun, F.; Wang, R.Q. Experimental investigation of the fracture evolution and fracture criterion of jointed sandstone subject to dry-wet cycling. *Bull. Eng. Geol. Environ.* **2023**, *82*, 101. [CrossRef]
52. Liu, S.; Jia, Y.; Zhai, Y.; Hao, S.X. Mesoscopic fracture damage evolution and fractal damage constitutive model of heat-treated red sandstone under direct tensile impact loadings. *J. Rock Mech. Geotech. Eng.* **2025**, *17*, 323–340. [CrossRef]

53. Zhelnin, M.; Kostina, A.; Prokhorov, A.; Plekhov, O.; Semin, M.; Levin, L. Coupled thermo-hydro-mechanical modeling of frost heave and water migration during artificial freezing of soils for mineshaft sinking. *J. Rock Mech. Geotech. Eng.* **2022**, *14*, 537–559. [CrossRef]
54. Sun, T.C.; Zhang, W.B.; Liu, J.; Dong, C.Q.; Yang, H.H.; Zhang, S. Effect of Roughness on the Shear Strength of Frozen Soil-Concrete Contact Surfaces in an Open Environment. *J. Cold Reg. Eng.* **2025**, *39*, 04025006. [CrossRef]
55. Meng, F.D.; Luo, Z.M.; Xie, Q.Y.; Zhai, Y. Study on structural deterioration characteristics and nonlinear dynamic damage constitutive model of freeze-thaw sandstone. *Results Eng.* **2026**, *29*, 109502. [CrossRef]
56. Liu, H.Y.; Lv, S.R.; Zhang, L.M.; Yuan, X.P. A dynamic damage constitutive model for a rock mass with persistent joints. *Int. J. Rock Mech. Min.* **2015**, *75*, 132–139. [CrossRef]
57. Wang, T.A.; Zhai, Y.; Gao, H.; Li, Y.B.; Zhao, R.F. A novel binary effective medium model to describe the prepeak stress-strain relationship of combined bodies of rock-like material and rock. *Int. J. Min. Sci. Technol.* **2023**, *33*, 601–616. [CrossRef]
58. Yang, Z.; Mou, X.Y.; Ji, H.L.; Liang, Z.H.; Zhang, J.H. Effects of freeze-thaw on bank soil mechanical properties and bank stability. *Sci. Rep.* **2024**, *14*, 9808. [CrossRef] [PubMed]
59. Azadi, A.; Momayez, M. Simulating a Weak Rock Mass by a Constitutive Model. *Mining* **2025**, *5*, 23. [CrossRef]
60. Melnikov, N.Y. *Geomechanical Substantiation of the Parameters of Quarries' Sides with Steep Layers Falling into the Massif in the Conditions of the Permafrost Zone*; Saint Petersburg Mining University: Saint Petersburg, Russia, 2019.